

A Discrete Adjoint Method for Two-Phase Condensing Flows Applied to the Shape Optimization of Turbine Cascades

Pini, M.; Azzini, L.; Vitale, S.; Colonna, Piero

DOI

[10.1115/1.4047781](https://doi.org/10.1115/1.4047781)

Publication date

2020

Document Version

Final published version

Published in

Journal of Turbomachinery

Citation (APA)

Pini, M., Azzini, L., Vitale, S., & Colonna, P. (2020). A Discrete Adjoint Method for Two-Phase Condensing Flows Applied to the Shape Optimization of Turbine Cascades. *Journal of Turbomachinery*, 142(11), Article TURBO-18-1308. <https://doi.org/10.1115/1.4047781>

Important note

To cite this publication, please use the final published version (if applicable). Please check the document version above.

Copyright

Other than for strictly personal use, it is not permitted to download, forward or distribute the text or part of it, without the consent of the author(s) and/or copyright holder(s), unless the work is under an open content license such as Creative Commons.

Takedown policy

Please contact us and provide details if you believe this document breaches copyrights. We will remove access to the work immediately and investigate your claim.

Green Open Access added to TU Delft Institutional Repository

'You share, we take care!' - Taverne project

<https://www.openaccess.nl/en/you-share-we-take-care>

Otherwise as indicated in the copyright section: the publisher is the copyright holder of this work and the author uses the Dutch legislation to make this work public.

M. Pini¹

Assistant Professor
Propulsion & Power Group,
Faculty of Aerospace Engineering,
Delft University of Technology,
Delft 2629HS, The Netherlands
e-mail: m.pini@tudelft.nl

L. Azzini

Propulsion & Power Group,
Faculty of Aerospace Engineering,
Delft University of Technology,
Delft 2629HS, The Netherlands
e-mail: l.azzini@tudelft.nl

S. Vitale

Propulsion & Power Group,
Faculty of Aerospace Engineering,
Delft University of Technology,
Delft 2629HS, The Netherlands
e-mail: s.vitale@tudelft.nl

P. Colonna

Professor
Propulsion & Power Group,
Faculty of Aerospace Engineering,
Delft University of Technology,
Delft 2629HS, The Netherlands
e-mail: p.colonna@tudelft.nl

A Discrete Adjoint Method for Two-Phase Condensing Flows Applied to the Shape Optimization of Turbine Cascades

This paper presents a fully turbulent two-phase discrete adjoint method for metastable condensing flows targeted to turbomachinery applications. The method is based on a duality preserving algorithm and implemented in the open-source CFD tool SU2. The optimization framework is applied to the shape optimization of two canonical steam turbine cascades, commonly referred to as White cascade and Dykas cascade. The optimization were carried out by minimizing either the liquid volume fraction downstream of the cascade or the total entropy generation due viscous effects and heat transfer. In the first case, the amount of condensate turned out to be reduced by as much as 24%, but without reduction of the generated entropy, while the opposite resulted in the second case. The outcomes demonstrate the capability and computational efficiency of adjoint-based automated design for the shape optimization of turbomachinery operating with phase change flow. [DOI: 10.1115/1.4047781]

Keywords: two-phase condensing flows, shape optimization, adjoint method, turbine aerodynamic design

1 Introduction

The adjoint method for aerodynamic shape optimization was first developed by Jameson [1] and since then it has been extensively applied to external flow design problems using either the continuous or the discrete adjoint (DA) formulation [2–4]. Its application to turbomachinery flows is relatively more recent, and its advantages in relation to such problems are less known. One of the reasons thereof is arguably due to the additional complexity of deriving the adjoint equations for wall-bounded flows, in particular regarding the linearization of complex boundary conditions like the non-reflective boundary conditions. This was especially the case in early time when most of the adjoint solvers were hand-derived. A further reason is arguably related to the challenge of attaining sufficiently converged solutions of the CFD simulations for turbomachinery flows, which greatly affects the convergence of the adjoint solver and the eventual accuracy of the calculated gradients. Adjoint-based optimization applied to turbomachinery design is documented for instance in Refs. [5–8].

The advent of automatic differentiation techniques based on operator overloading [9] has opened up the possibility of efficiently performing the differentiation of complex CFD scripts in a black-box fashion, provided that the solver is implemented in such a way that it allows the linearization of all the routines in a sequential manner. If any piece of the code can be automatically differentiated, one can focus on implementing new physical models and numerical algorithms in the flow solver, while being able to obtain its adjoint counterpart almost automatically.

The open-source SU2 solver [10] is becoming increasingly popular within the CFD community because it implements a flexible, accurate, and efficient DA solver [9]. The DA solver is

automatically derived by means of advanced algorithmic differentiation (AD) techniques [11]. Various applications of this new design framework have been presented. In Ref. [9], the authors described an application of the SU2 DA solver to external aerodynamic problems. Reference [12] documents the application of the method to the design of aircraft wings, taking into account aeroacoustic constraints, while the solution of aero elastic design problems is treated in Ref. [13]. Reference [14] illustrates the extension of the adjoint framework to design problems involving more complex fluid flows, namely the aerodynamic performance optimization of organic Rankine cycle (ORC) turbine cascades. Aerodynamic shape optimization accounting for the fully turbulent and unsteady nature of flows is reported in Ref. [15]. The approximation of the harmonic balance method allows in this case to keep the computational time within feasible limits.

This paper documents the extension of the SU2 design framework to turbomachinery flow problems characterized by phase change. Specifically, the focus here is on vapor flows condensing at non-equilibrium thermodynamic conditions [16]. This type of flows occur, among others, in the last stages of steam turbines [17] or in centrifugal compressors operating with supercritical carbon dioxide [18] and lead to aero-mechanical performance degradation. For example, droplet formation is a highly irreversible process leading to a work reduction of up to 1–2% for each stage of large steam turbines in which condensation occurs [19]. The performance of turbomachinery affected by fluid condensation can be improved by re-shaping blades using automated design algorithms in combination with high-fidelity, two-phase CFD models.

According to open literature, a limited body of research deals with shape optimization of turbomachinery components operating with condensing flows [20,21], arguably due to the challenges and the computational cost associated with the two-phase flow simulations. The objective of this work is to develop and demonstrate the capability of a computationally efficient design approach based on the adjoint method. To this end, the adjoint-based shape optimization method for single phase turbulent flows implemented

¹Corresponding author.

Contributed by the Heat Transfer Division of ASME for publication in the JOURNAL OF TURBOMACHINERY. Manuscript received October 30, 2018; final manuscript received May 9, 2020; published online September 18, 2020. Assoc. Editor: Dr. Paul Durbin.

in the SU2 solver has been extended to account for the occurrence of non-equilibrium condensation using the method of moments [22]. The method is based on a duality-preserving approach, which guarantees that the two-phase adjoint solver inherits the same iterative convergence behavior of the primal flow solver. The capability and computational performance of the novel two-phase design method are illustrated by describing the shape optimization of two exemplary steam turbine cascades.

2 Numerical Model

2.1 Flow Solver. The governing equations of the two-phase flow are formulated by adopting the so-called Eulerian formulation. The vapor flow is modeled with the equations of mass, momentum, and energy conservation, while source terms are used for the coupling between the two phases. The vapor equations for turbulent flow are

$$\begin{cases} \frac{\partial \rho_v}{\partial t} + \nabla \cdot (\rho_v \mathbf{v}) = S_v \\ \frac{\partial \rho_v v_x}{\partial t} + \nabla \cdot (\rho_v v_x \mathbf{v}) + \frac{\partial P}{\partial x} = \nabla \cdot \boldsymbol{\tau}_x + S_{SA,v_x} + S_v v_x \\ \frac{\partial \rho_v v_y}{\partial t} + \nabla \cdot (\rho_v v_y \mathbf{v}) + \frac{\partial P}{\partial y} = \nabla \cdot \boldsymbol{\tau}_y + S_{SA,v_y} + S_v v_y \\ \frac{\partial (\rho_v e_{0,v})}{\partial t} + \nabla \cdot (\rho_v h_{0,v} \mathbf{v}) = \nabla \cdot (\boldsymbol{\tau} \mathbf{v}) + S_{SA,e} + S_v h_{0,1} \end{cases} \quad (1)$$

where ρ_v , P , $e_{0,v}$ and $h_{0,v}$ are the density, pressure total energy, and total enthalpy of the vapor. Additionally, $h_{0,1}$ is the liquid total enthalpy, $v_{x,y}$ are the velocity components, $\boldsymbol{\tau}$ is the viscous tensor, and $S_{SA,v_x,v_y,e}$ are the turbulent source terms, determined through the Spalart–Allmaras turbulence model [23]. Finally, S_v is the source term that represents the exchange of mass between the liquid and the vapor phases, and it is defined as

$$S_v = -\rho_m \frac{3y_{\text{mass}}}{R} \frac{\partial R}{\partial t} \quad (2)$$

in which y_{mass} and R are the liquid mass fraction and the droplet average radius, respectively, and ρ_m is the mixture density.

The liquid phase is described by using the method of moments proposed by Hill [22], which essentially results in a set of conservation laws for the droplet radius distribution function. The equations are cast in the following form:

$$\begin{cases} \frac{\partial}{\partial t} (\rho_m \mu_0) + \nabla \cdot (\rho_m \mu_0 \mathbf{v}) = \rho_m J(R_*) \\ \frac{\partial}{\partial t} (\rho_m \mu_1) + \nabla \cdot (\rho_m \mu_1 \mathbf{v}) = \rho_m J(R_*) R_* + \mu_0 G \\ \frac{\partial}{\partial t} (\rho_m \mu_2) + \nabla \cdot (\rho_m \mu_2 \mathbf{v}) = \rho_m J(R_*) R_*^2 + 2\mu_1 G \\ \frac{\partial}{\partial t} (\rho_m \mu_3) + \nabla \cdot (\rho_m \mu_3 \mathbf{v}) = \rho_m J(R_*) R_*^3 + 3\mu_2 G \end{cases} \quad (3)$$

where μ_j is the generic moment of order j . The terms J , G , and the critical radius R_* are reported in Appendix.

The liquid properties are retrieved by assuming mechanical equilibrium, thus equal static pressure of the two-phases, and kinematic equilibrium, hence no slip, between the liquid and the vapor phase. The liquid temperature T_1 is evaluated through the capillarity model reported in Appendix.

The equations are used to simulate steady-state test-cases. Both sets of equations are discretized using second-order spatial discretization schemes and integrated in time using first-order implicit time integration in a segregated manner. The current two-phase flow model is implemented in the open-source SU2 code [10].

2.2 Adjoint Solver. The set of governing equations (1) and (3) written in compact form reads

$$\frac{\partial \mathbf{U}}{\partial t} + \nabla \cdot (\mathbf{F}^c + \mathbf{F}^v) = \mathbf{Q} \quad (4)$$

$$\mathbf{U} = \begin{bmatrix} U_{\text{flow}} \\ U_{2\text{phase}} \\ U_{\text{turb}} \end{bmatrix}, \quad \mathbf{F}^c = \begin{bmatrix} F_{\text{flow}}^c \\ F_{2\text{phase}}^c \\ F_{\text{turb}}^c \end{bmatrix}, \quad \mathbf{F}^v = \begin{bmatrix} F_{\text{flow}}^v \\ 0 \\ F_{\text{turb}}^v \end{bmatrix}, \quad \mathbf{Q} = \begin{bmatrix} Q_{\text{flow}} \\ Q_{2\text{phase}} \\ Q_{\text{turb}} \end{bmatrix} \quad (5)$$

where \mathbf{U} indicates the vector containing the conservative variables of (1) and (3) and the turbulent equations \mathbf{F}^c and \mathbf{F}^v represent the convective and viscous fluxes, respectively, and \mathbf{Q} the source terms. For a steady-state problem, the solution of Eq. (4) at time $n+1$, i.e. \mathbf{U}^{n+1} , in case an implicit integration scheme is adopted, can be expressed as

$$\mathbf{U}^{n+1} = \mathbf{U}^n + \Delta \mathbf{U}^n = \mathbf{U}^n - \mathbf{P}^{-1} \mathbf{R}(\mathbf{U}^n, \mathbf{X}) \quad (6)$$

in which \mathbf{R} is the residual vector of the equations, \mathbf{X} denotes the vector of grid points of the domain, and the preconditioning matrix \mathbf{P} is the Jacobian of the flow and turbulent equations. Equation (6) can be reformulated in terms of fixed point iteration as

$$\mathbf{U}^{n+1} = \mathcal{G}(\mathbf{U}^n, \mathbf{X}) \quad (7)$$

According to the Banach fixed-point theorem [24], Eq. (6) admits a unique converged solution \mathbf{U}^* if \mathcal{G} is contractive, i.e., $\|\mathcal{G}\| < 1$.

The aerodynamic design problem can be formulated by including in the notation the explicit dependence of the objective function \mathcal{J} from the vector of the design variables, resulting in

$$\begin{aligned} \min \quad & \mathcal{J}(\boldsymbol{\alpha}, \mathbf{U}(\boldsymbol{\alpha}), \mathbf{X}(\boldsymbol{\alpha})) \\ \text{subject to} \quad & \mathbf{U}(\boldsymbol{\alpha}) = \mathcal{G}(\mathbf{U}(\boldsymbol{\alpha}), \mathbf{X}(\boldsymbol{\alpha})) \\ & \mathbf{X}(\boldsymbol{\alpha}) = \mathbf{M}(\boldsymbol{\alpha}) \end{aligned} \quad (8)$$

where $\mathbf{M}(\boldsymbol{\alpha})$ is a differentiable function denoting the mesh deformation algorithm. The Lagrangian of the constrained optimization problem L can be then written as

$$\begin{aligned} L(\boldsymbol{\alpha}, \mathbf{U}(\boldsymbol{\alpha}), \mathbf{X}(\boldsymbol{\alpha}), \boldsymbol{\lambda}, \boldsymbol{\mu}) = & \mathcal{J}(\mathbf{U}(\boldsymbol{\alpha}), \mathbf{X}(\boldsymbol{\alpha}), \boldsymbol{\alpha}) \\ & + (\mathcal{G}(\mathbf{U}(\boldsymbol{\alpha}), \mathbf{X}(\boldsymbol{\alpha})) - \mathbf{U}(\boldsymbol{\alpha}))^T \boldsymbol{\lambda} \\ & + (\mathbf{M}(\boldsymbol{\alpha}) - \mathbf{X}(\boldsymbol{\alpha}))^T \boldsymbol{\mu} \end{aligned} \quad (9)$$

where $\boldsymbol{\lambda}$ and $\boldsymbol{\mu}$ are the Lagrangian multipliers or adjoint variables. The differential of the lagrangian function with respect to the vector of the design variables $\boldsymbol{\alpha}$ yields

$$dL = \frac{\partial L}{\partial \boldsymbol{\alpha}} d\boldsymbol{\alpha} + \frac{\partial L}{\partial \mathbf{U}(\boldsymbol{\alpha})} \frac{\partial \mathbf{U}(\boldsymbol{\alpha})}{\partial \boldsymbol{\alpha}} d\boldsymbol{\alpha} + \frac{\partial L}{\partial \mathbf{X}(\boldsymbol{\alpha})} \frac{\partial \mathbf{X}(\boldsymbol{\alpha})}{\partial \boldsymbol{\alpha}} d\boldsymbol{\alpha} \quad (10)$$

thus, omitting the explicit dependence from the independent variables, it reads

$$\begin{aligned} \frac{dL}{d\boldsymbol{\alpha}} = & \frac{\partial \mathcal{J}}{\partial \boldsymbol{\alpha}} + \left[\frac{\partial \mathcal{J}}{\partial \mathbf{U}} + \left(\frac{\partial \mathcal{G}}{\partial \mathbf{U}} \right)^T \boldsymbol{\lambda} - \boldsymbol{\lambda} \right] \frac{\partial \mathbf{U}}{\partial \boldsymbol{\alpha}} \\ & + \left[\frac{\partial \mathcal{J}}{\partial \mathbf{X}} + \left(\frac{\partial \mathcal{G}}{\partial \mathbf{X}} \right)^T \boldsymbol{\lambda} - \boldsymbol{\mu} \right] \frac{\partial \mathbf{X}}{\partial \boldsymbol{\alpha}} + \left(\frac{\partial \mathbf{M}}{\partial \boldsymbol{\alpha}} \right)^T \boldsymbol{\mu} \end{aligned} \quad (11)$$

from which the adjoint equations are derived as

$$\frac{\partial \mathcal{J}}{\partial \mathbf{U}} + \left(\frac{\partial \mathcal{G}}{\partial \mathbf{U}} \right)^T \boldsymbol{\lambda} - \boldsymbol{\lambda} = 0 \quad (12)$$

and

$$\frac{\partial \mathcal{J}}{\partial \mathbf{X}} + \left(\frac{\partial \mathcal{G}}{\partial \mathbf{X}} \right)^T \boldsymbol{\lambda} - \boldsymbol{\mu} = 0 \quad (13)$$

Similarly to the flow solver (7), (12) can be solved with a fixed-point iteration scheme in λ , namely

$$\lambda^{n+1} = \frac{\partial \mathcal{J}}{\partial U} + \left(\frac{\partial \mathcal{G}}{\partial U} \right)^T \lambda^n = \mathcal{N}(\lambda^n, U^*, X) \quad (14)$$

where U^* is the numerical solution of the two-phase flow equations. Since \mathcal{N} is contractive, Eq. (14) will converge at the same rate as the primal flow solver when using the same time-marching scheme. The right hand-side of Eq. (14) is obtained by resorting to Algorithmic Differentiation applied to the source code of the program that computes \mathcal{J} and \mathcal{G} in black-box fashion. This is made possible at the expense of a small runtime overhead by the use of the *Jacobi taping method* implemented in the AD tool CODIPACK [25] in combination with the *Expression Templates* feature of C++. Equation (13) is instead evaluated only once the adjoint solution vector has been computed. Finally, by replacing Eqs. (12), (13) in (11), one obtains the gradient of the objective function \mathcal{J} with respect of the design variables $M(\alpha)$ as

$$\frac{dL}{d\alpha} = \frac{d\mathcal{J}}{d\alpha} = \frac{\partial \mathcal{J}}{\partial \alpha} + \frac{\partial M^T}{\partial \alpha} \mu \quad (15)$$

The same approach is used to calculate the gradients of any of the constraints of the optimization problem featuring explicit dependence on the design variables. A full description of the aerodynamic design chain can be found in Refs. [9,14]. Both the two-phase flow and adjoint solvers can be run in serial or parallel mode using a mesh partitioning approach and an implementation of the message-passing interface standard.

3 Thermodynamic Modeling of the Two-Phase Fluid

The thermo-physical fluid properties are computed by means of specific fluid models, depending on the thermodynamic region, because these algebraic equations can easily be differentiated. The equilibrium and metastable thermodynamic properties of the vapor phase states are computed by means of a thermodynamic model based on an improved Peng–Robinson equation of state (EoS) [26] directly implemented in SU2. Viscosity and thermal conductivity are computed by the same library in correspondence with the total conditions P_0, T_0 at the nozzle inlet and kept constant along the expansion.

The liquid density is taken from Ref. [27], while the liquid enthalpy is calculated by subtracting the value of the latent heat of vaporization from the value of the saturated vapor enthalpy at the vapor temperature T_v . The calculated properties are therefore thermodynamically inconsistent, namely, the value of saturated pressure and temperature calculated with the liquid model are slightly different from the same properties if calculated with the vapor model. However, this has no influence on the numerics and the accuracy of the results, as demonstrated by the results shown in Sec. 5. Finally, the surface tension is evaluated using the relations given in Ref. [28]. All these models are implemented in SU2 to enhance the computational efficiency of the two-phase numerical model.

4 Objective Function for Turbomachinery Design Problems With Condensing Flows

A comprehensive review of loss mechanisms associated with metastable condensation in turbomachinery is provided in Ref. [29]. The largest share of entropy generation due to non-equilibrium condensation is due to heat transfer between the liquid and the vapor phase and this loss is usually termed *thermodynamic wetness loss*. Furthermore, the formation of tiny liquid droplets generally leads to pitting and erosion of the blades leading-edge, which eventually may affect their structural integrity, thus, the final performance [29,30]. Stemming from these

considerations, the objective function \mathcal{J} for the two-phase adjoint-based optimization framework can be defined in terms of (i) minimization of liquid volume fraction y_{vol} in order to reduce the amount of liquid condensate (ii) and minimization of entropy loss coefficient ζ in order to mitigate all irreversible flow phenomena, thus including those due to non-equilibrium condensation. The way in which the two objective functions are calculated from CFD results is described in the following.

4.1 Liquid Volume Fraction. The liquid volume fraction y_{vol} can be directly computed from the transport equation of the third moment μ_3 as

$$y_{vol} = \frac{4\pi}{3} U_{2\text{phase},4} = \frac{4}{3} \pi \rho_m \mu_3 \quad (16)$$

An averaged value of this quantity suited as objective function is obtained by applying mass-flow averaging to the non-uniform y_{vol} distribution at the outflow boundary. Due to the order of magnitude of $U_{2\text{phase},4}$, i.e., approximately 1×10^{-6} , the calculations were run until the residual of the last transport equation of the second phase was at least lower than 1×10^{-10} .

The quantity y_{vol} was selected over the liquid mass fraction y_{mass} , defined as

$$y_{mass} = \frac{4}{3} \pi U_{2\text{phase},4} \frac{\rho_l}{\rho_m} = \frac{U_{2\text{phase},4} \rho_l}{U_{2\text{phase},4} (\rho_l - \rho_v) + (3/4\pi) \rho_v} \quad (17)$$

to avoid numerical issues related to the different order of magnitude of the terms at the denominator of Eq. (17).

4.2 Entropy Loss Coefficient. Using first principles, for a fixed control volume in which the condensing vapor flows through, the entropy generation Δs due to loss mechanisms can be computed as

$$\Delta s = s_{out} - s_{in} \quad (18)$$

in which

$$s_{out} = y_{mass,out} s_{l,out} + (1 - y_{mass,out}) s_{v,out} \quad (19)$$

$s_{l,out}$ are the liquid and the vapor entropy fluxes at the outlet boundary of the control volume. s_{in} is the entropy flux of the inlet flow stream, determined starting from the inlet total conditions P_0, T_0 assuming single phase in thermodynamic equilibrium conditions. $y_{mass,out}$ is the liquid mass fraction per unit mass. The entropy loss coefficient ζ is finally expressed as

$$\zeta = \Delta s \frac{T_{out,s}}{\frac{1}{2} v_{out}^2} \quad (20)$$

where $T_{out,s}$ and v_{out} are the outlet static temperature and flow absolute velocity.

In all calculations, the entropy values at inlet and outlet boundaries are obtained by applying mass-flow averaging to the non-uniform flow. The use of a coefficient lumping all dissipative contributions coming from viscous effects, shock waves, and thermodynamic wetness losses is a convenient choice in turbomachinery applications as loss mechanisms are seldom independent and performance parameters eventually depend on global entropy increase.

For either objective functions, the optimization runs were conducted using the Sequential Least Squares Programming (SLSQP) optimizer described in Ref. [31].

5 Applications

The capability of the adjoint-based design framework is demonstrated by performing shape optimization of two exemplary steam

Table 1 Dykas cascade: boundary conditions, and simulation parameters

P_0 (Pa)	T_0 (K)	P_{out} (Pa)	μ (Pa·s)	k (W mK ⁻¹)	μ_{turb}/μ	I
0.89×10^5	373.15	0.39×10^5	12.252×10^{-6}	24.626×10^{-3}	100	0.05

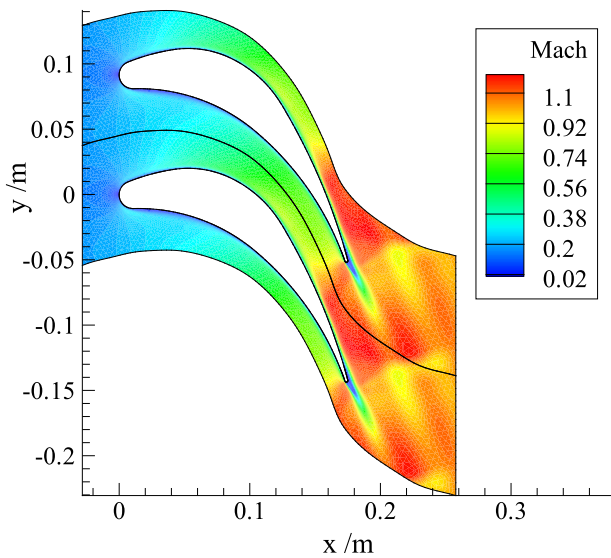


Fig. 1 Dykas cascade: Mach number distribution within the flow field

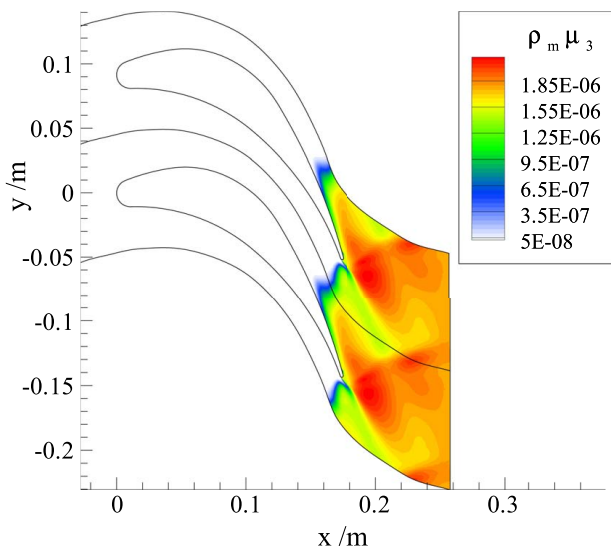


Fig. 2 Dykas cascade: $U_{2phase,4}$ distribution within the flow field

cascades made of blades that are representative of typical blade profiles for steam turbines. The first blades row corresponds to the stator of the last stage of a 200 MW_e steam turbine [32], while the second one is taken from the fifth stage of an industrial steam turbine of large power capacity and is described in Ref. [33]. The illustration of the test cases follows the same structure. First, it is reported the validation of the numerical model. Then, the results of the optimization using the two objective functions are discussed. For the sake of clarity, the two turbine cascades are referred to as the *Dykas cascade* and the *White cascade* in the following, from the name of the first author of the paper where the experimental

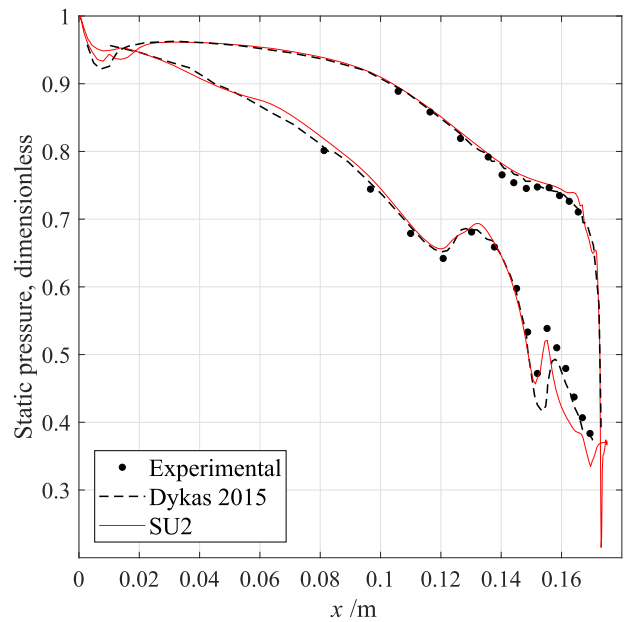


Fig. 3 Dykas cascade: pressure distribution on the blade surface. Comparison between simulation results and the experimental data in Ref. [32].

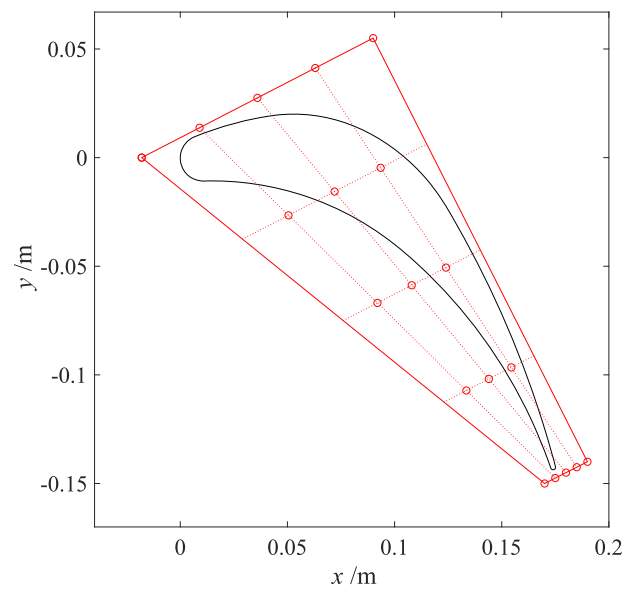


Fig. 4 Dykas cascade: blade profile and FFD box control points

studies were published. It is assumed that both the considered low-pressure steam turbine cascades were designed using best design practices for condensing flows in steam turbines.

5.1 Dykas Cascade

5.1.1 Validation of the Numerical Model. The boundary conditions and the simulation parameters are listed in Table 1. Simulations were run using second-order numerical schemes on a mesh comprising 30 k elements. The CFL number was set to 20 and kept constant during the simulation.

The contour of the Mach field and liquid volume fraction is shown in Figs. 1 and 2. The condensation onset occurs right after the impingement of the expansion fan on the suction side. The release of latent heat in the supersonic flow stream induces the formation of a condensation shock at about $x = 0.16$ m, followed by a

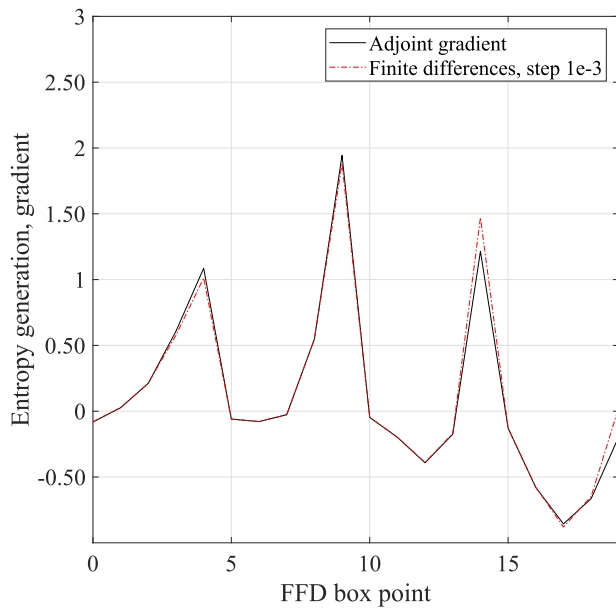


Fig. 5 Dykas cascade: comparison between the entropy generation gradient calculated with the adjoint solver and the same quantity calculated with finite differences

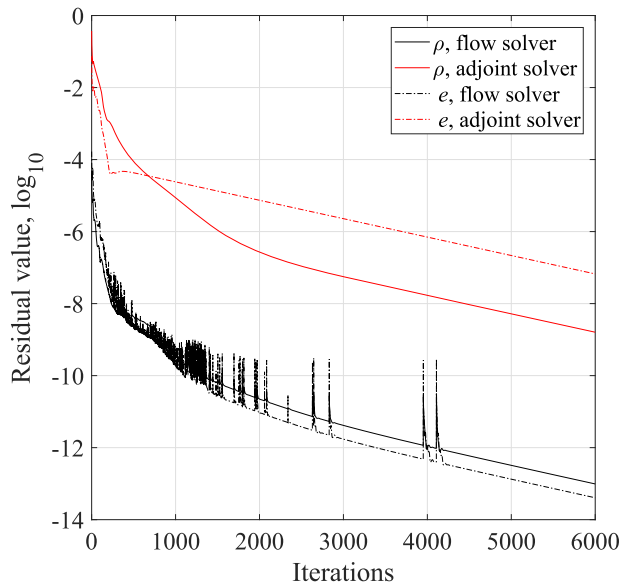


Fig. 6 Dykas cascade: convergence history of the solutions $U_{flow,1}$ and $U_{flow,4}$

further flow expansion up to the trailing edge. The pressure distribution along the blade surface obtained by the numerical model is compared to that obtained experimentally in Fig. 3. It can be observed that the largest deviations are located in correspondence of the so-called condensation shock. However, the location of condensation inception, i.e., the Wilson point, is correctly predicted by the model. Overall, the accuracy of the model is deemed adequate for design purposes.

The adjoint solver is validated by comparing the gradient of the objective function against the one computed by centered finite differences (FD) with a step size of 1×10^{-3} . The blade is parametrized using an FFD (Free-Form Deformation) box constituted by 25 control points, see Fig. 4. These are the design variables of the vector α used to define the optimization problem.

Figure 5 shows that the gradients of the entropy loss coefficient computed by the adjoint method are well in agreement with the

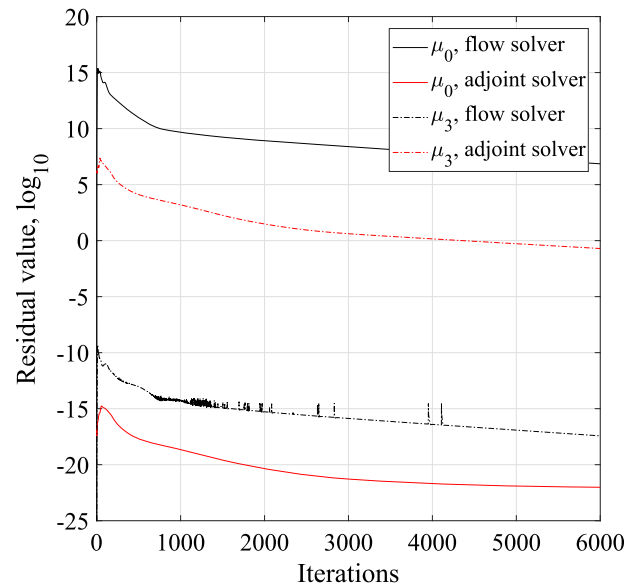


Fig. 7 Dykas cascade: convergence history of the solutions $U_{2phase,1}$ and $U_{2phase,4}$

Table 2 Dykas cascade: physical time and peak memory allocated required for (i) single-phase laminar (1ph, visc), (ii) single-phase turbulent (1ph, turb), (iii) adjoint single-phase turbulent (Adj 1ph, turb), (iv) two-phase turbulent (2ph, turb) and (v) adjoint two-phase turbulent (Adj 2ph, turb) simulations

	1ph, visc	1ph, turb	adj 1ph turb	2ph, turb	Adj 2ph, turb
Rel. time	1	1.12	1.58	1.26	3.06
Max memory	1	1.05	3.96	1.92	5.26

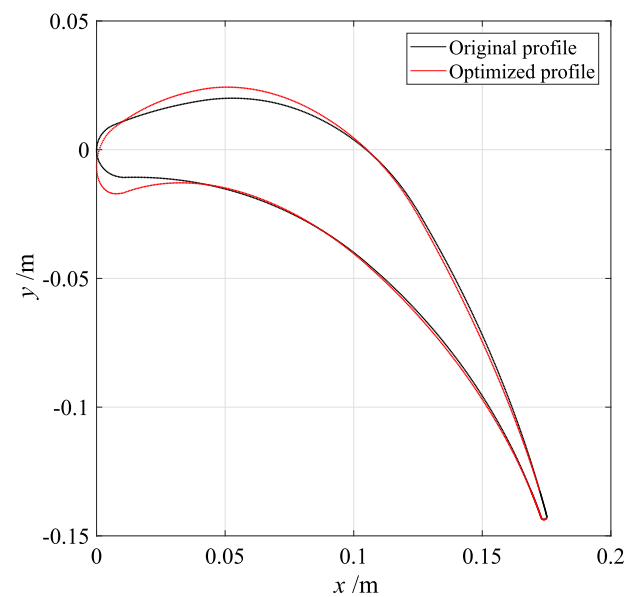


Fig. 8 Dykas cascade: comparison between the original profile and the optimized profile in case the objective is the minimization of the liquid volume fraction

correspondent FD values. Additionally, Figs. 6 and 7 depict the convergence history of both solvers. The use of the duality-preserving approach allows the adjoint solver to inherit the same convergence rate of the primal solver.

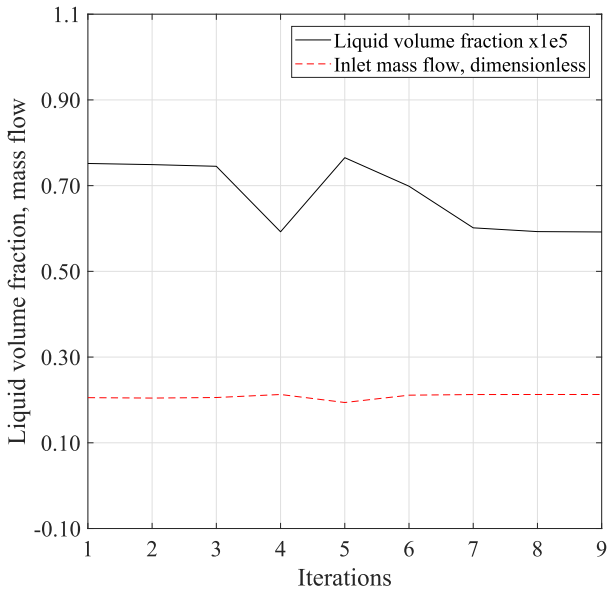


Fig. 9 Dykas cascade: optimization history in case the objective is the minimization of the liquid volume fraction

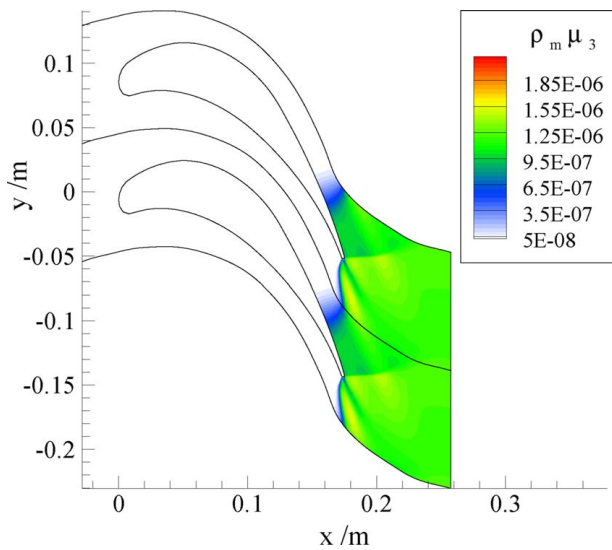


Fig. 10 Dykas cascade: $U_{2\text{phase},4}$ distribution for the optimized profile in case the objective is the minimization of the liquid volume fraction

The computational cost and peak memory requirement of the two-phase numerical model are normalized with the values of a single phase viscous computation and summarized in Table 2. If compared with the performance of a single-phase turbulent model, the extra cost demanded by the two-phase model is of the order of 20% for the flow and two times higher for the adjoint solver, while in terms of memory requirement the increase is of the same order of magnitude.

5.1.2 Shape Optimization. The simulated performance for the *Dykas cascade* was optimized under the constraint of preserving the baseline mass flow rate. The resulting optimization problem is then set as follows:

$$\begin{aligned} & \underset{\alpha}{\text{minimize}} && \gamma_{\text{vol}}(\alpha), \zeta(\alpha) \\ & \text{subject to:} && \dot{m} = \dot{m}_b \end{aligned} \quad (21)$$

The outcomes of the optimization achieved by minimizing the liquid volume fraction are discussed first. Figures 8 and 9 illustrate

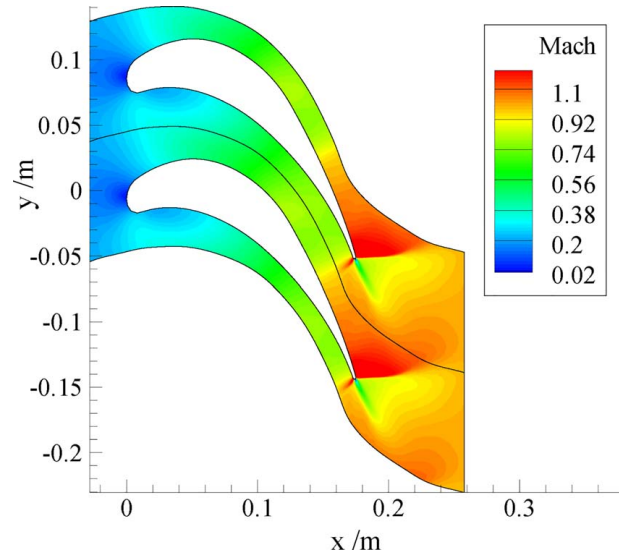


Fig. 11 Dykas cascade: Mach number distribution for the optimized profile in case the objective is the minimization of the liquid volume fraction

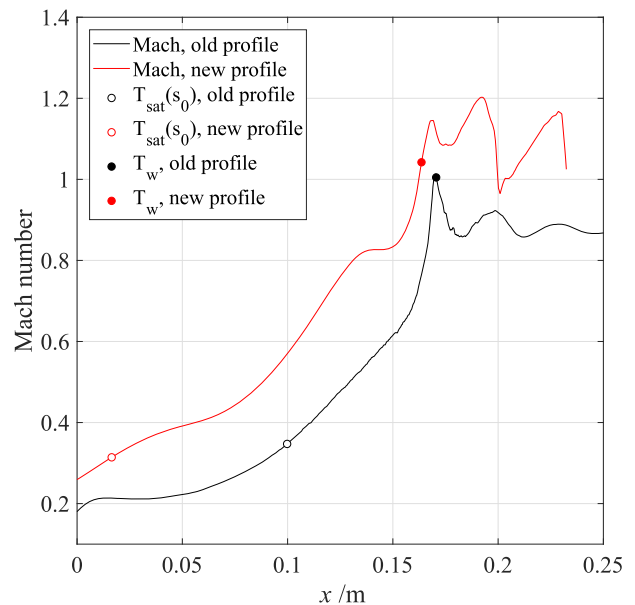


Fig. 12 Dykas cascade: comparison between the averaged streamwise Mach number distribution for the original profile and the optimized profile in case the objective is the minimization of the liquid volume fraction

the original and optimized blade profile and the convergence history of the optimization, respectively. As it can be observed, the automated shape optimization allowed to reduce the liquid volume fraction by about 20% in six design iterations. This is also evident from the contour of the third moment μ_3 displayed in Fig. 10.

Figure 11 shows the Mach number contour of the optimized cascade, while Fig. 12 shows the distribution of the mass-flow averaged Mach number in the streamwise direction. The latter figure is reported in order to support insights on the physical cause of lower liquid volume level calculated for the optimized cascade. The reshape of the leading edge provided by the optimization entails larger flow over-speed in the aft-part of the blade, which causes the vapor to undergo larger excursion into the metastable region. The net result is a delay of condensation onset which leads to a larger number of tiny droplets to form in the region downstream

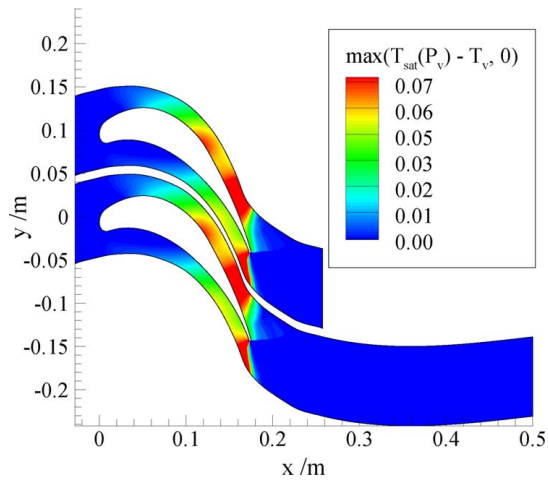


Fig. 13 Dykas cascade: degree of subcooling ΔT_{sub} for the simulations with the optimized profile in case the objective is the minimization of the liquid volume fraction, comparison between short (up) and extended domain (down)

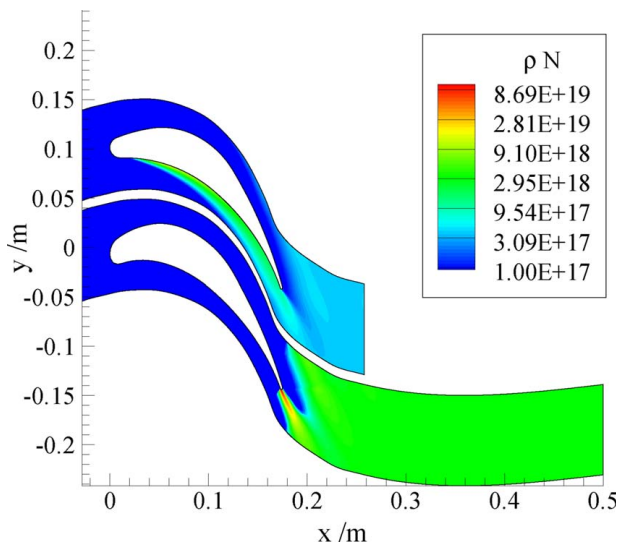


Fig. 14 Dykas cascade: $U_{2\text{phase},1}$ for the original profile (up) and the optimized profile in case the objective is the minimization of the liquid volume fraction (down)

of the blade. However, the reduction of liquid volume fraction obtained by shaping the leading-edge comes at the expense of a higher degree of vapor subcooling, which directly affects the fluid-dynamic performance of the cascade, i.e., the higher the subcooling the higher the fluid-dynamic losses. For the optimized cascade, the thermodynamic wetness loss increases by approximately 12% with respect to the baseline cascade when the flow reverts back to thermodynamic equilibrium at the outflow boundary. A further simulation performed with an extended flow domain confirmed that thermodynamic equilibrium conditions are practically met at an axial distance lower than a typical stator-rotor clearance in axial turbines. Figure 13 reports the degree of subcooling, defined as

$$\Delta T_{\text{sub}} = T_{\text{sat}}(P_v) - T_v \quad (22)$$

obtained for the original and optimized profile with the extended domain, whereas Fig. 14 displays the solution $U_{2\text{phase},1}$, given by

$$U_{2\text{phase},1} = \rho_m N \quad (23)$$

where N is the average number of droplets, for the original profile and the optimized case.

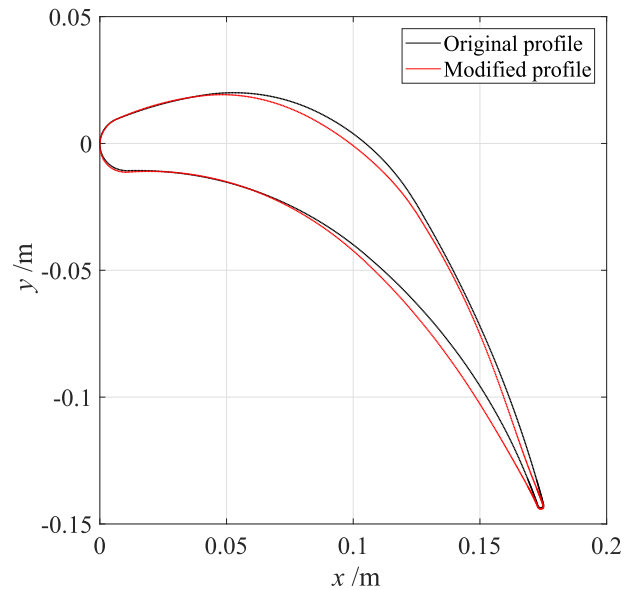


Fig. 15 Dykas cascade: comparison between the original profile and the optimized profile in case the objective is the minimization of the thermodynamic losses

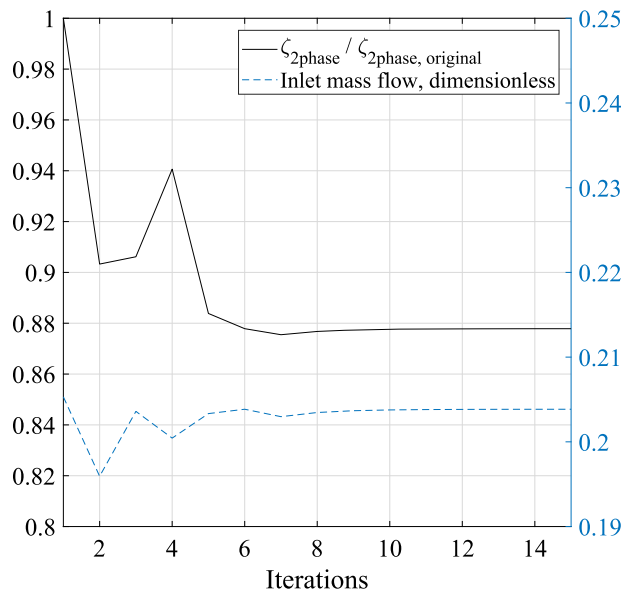


Fig. 16 Dykas cascade: optimization history in case the objective is the minimization of the thermodynamic losses

From the previous findings, it can be inferred that a reduction of liquid volume fraction does not directly yield an improvement of cascade fluid-dynamic efficiency, which instead is attainable by minimizing the entropy coefficient. The results of this second optimization are reported in Figs. 15 and 16. The loss coefficient is reduced by about 11%, but the liquid volume fraction turned out to increase by about 3%. Figures 17 and 18 report the simulation results in terms of Mach number and liquid volume fraction contour. This result suggests that, for the problem at hand, a simultaneous reduction of liquid volume fraction and entropy generation can be obtained only by concurrently minimizing both objectives.

The fluid-dynamic performance gain is found to be due to improved aerodynamic characteristics of the blade as well as a reduction of vapor subcooling throughout the channel, as visible from the contour of vapor subcooling and blade pressure distribution in Figs. 19 and 20.

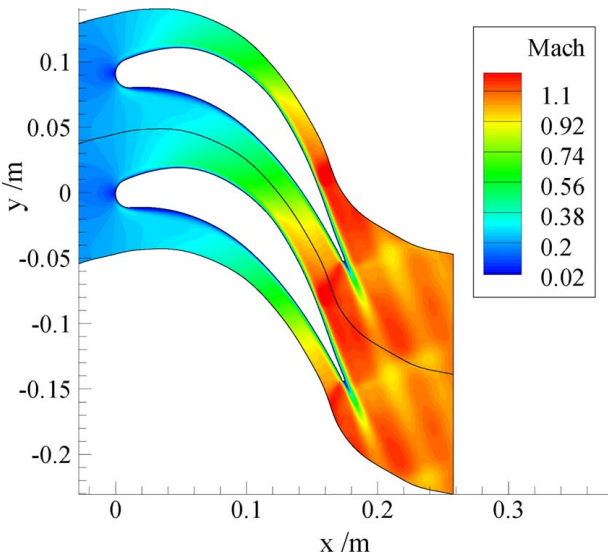


Fig. 17 *Dykas cascade*: Mach number distribution for the optimized profile in case the objective is the minimization of the thermodynamic losses

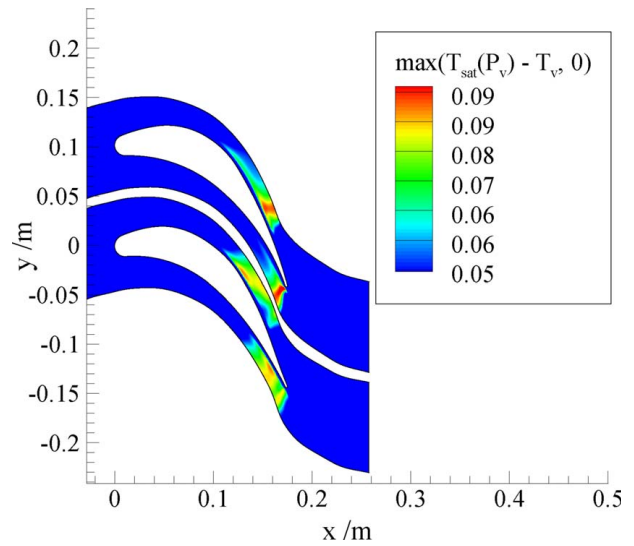


Fig. 19 *Dykas cascade*: comparison between the vapor sub-cooling of the original blade (up) and that of the optimized profile in case the objective is the minimization of the thermodynamic losses (down)

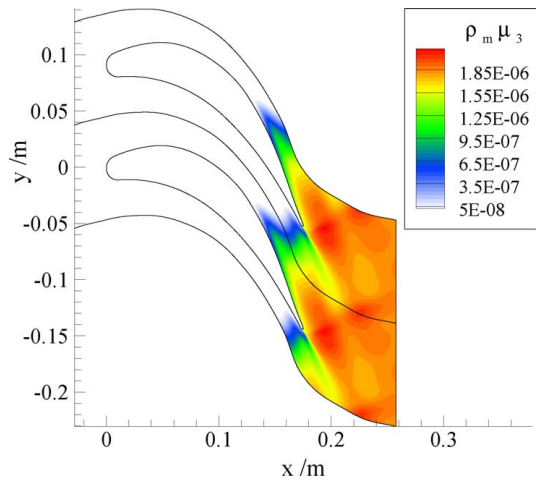


Fig. 18 *Dykas cascade*: $U_{2\text{phase},4}$ distribution for the optimized profile in case the objective is the minimization of the thermodynamic losses

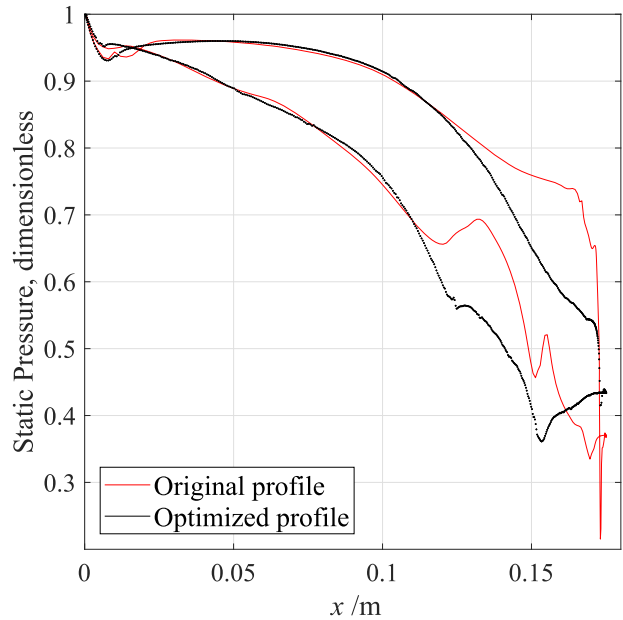


Fig. 20 *Dykas cascade*: blade loading of the baseline and optimized configuration in case the objective is the minimization of the thermodynamic losses

5.2 White Cascade

5.2.1 Validation of the Numerical Model. The boundary conditions and the simulation parameters for the second test case are reported in Table 3. The number of mesh elements and the CFL number were set equal to the previous case.

Figure 21 shows the comparison between the blade load obtained from the simulations and the experimental data in Ref. [33]. Figures 22 and 23 display the results of the two-phase simulation. Similarly to the results obtained with the *Dykas cascade*, the condensation onset is predicted with sufficient accuracy, while the pressure distribution on the rear suction side shows the largest deviations as compared to the experimental data. This is attributed to an over estimation of the amount of latent heat released after condensation onset, which causes a more pronounced pressure peak followed by a smoother flow expansion before the final recompression.

Figures 24 and 25 show the FFD box used for the optimization and the adjoint gradient validation. As for the previous case, the gradients obtained by adjoint and second-order finite differences are well in accordance.

5.2.2 Shape Optimization. The minimization of the liquid volume fraction and entropy loss coefficient was carried out by imposing an inequality constraint on the averaged outlet flow angle. The optimization problem is then formulated as

$$\begin{aligned} & \underset{\alpha}{\text{minimize}} && y_{\text{vol}}(\alpha), \zeta(\alpha) \\ & \text{subject to:} && \alpha > \alpha_b \end{aligned} \quad (24)$$

Figures 26 and 27 depict the optimal profile and the convergence history when minimizing the liquid volume fraction. The optimal profile is characterized by a liquid volume fraction reduced by 25% with respect to the original case. The contour of Mach number and volume fraction is reported in Figs. 28 and 29.

Table 3 White cascade: boundary conditions, and simulation parameters

P_0 (Pa)	T_0 (K)	P_{out} (Pa)	μ (Pa·s)	k (W/m/K)	μ_{turb}/μ	I
0.409×10^5	354.0	0.196×10^5	11.579×10^{-6}	22.971×10^{-3}	100	0.05

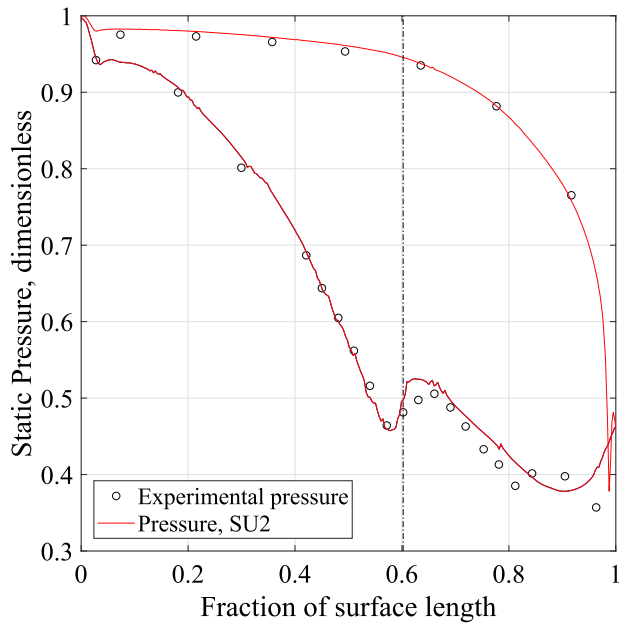


Fig. 21 White cascade: pressure distribution on the blade surface, comparison between the simulation results and the experimental data in Ref. [33]

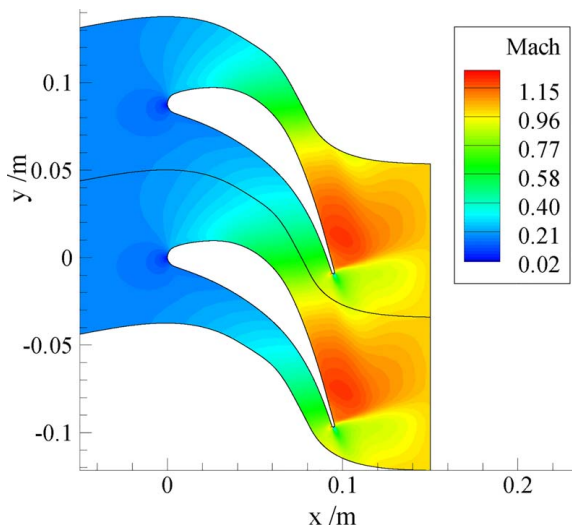


Fig. 22 White cascade: Mach number distribution within the flow field

As opposed to the results obtained with the *Dykas cascade*, the flow reaches thermodynamic equilibrium at approximately one chord downstream of the cascade. Figure 30 shows the subcooling ΔT_{sub} for the optimized profile resulting from the use of (i) a short and (ii) an extended simulation domain. The thermodynamic wetness losses for the optimized profile calculated using an extended flow domain are comparable to those of the original

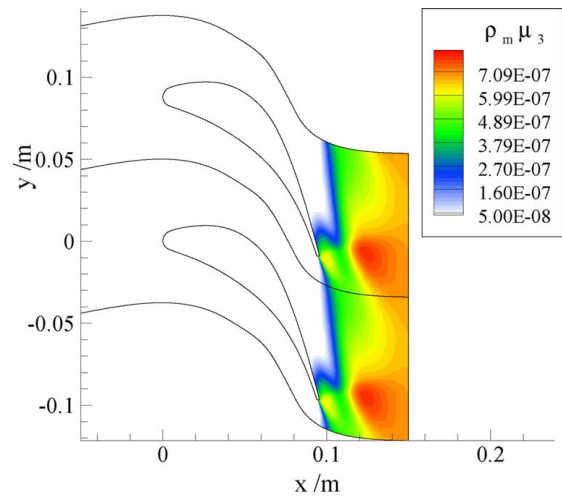


Fig. 23 White cascade: $U_{2phase,4}$ distribution within the flow field

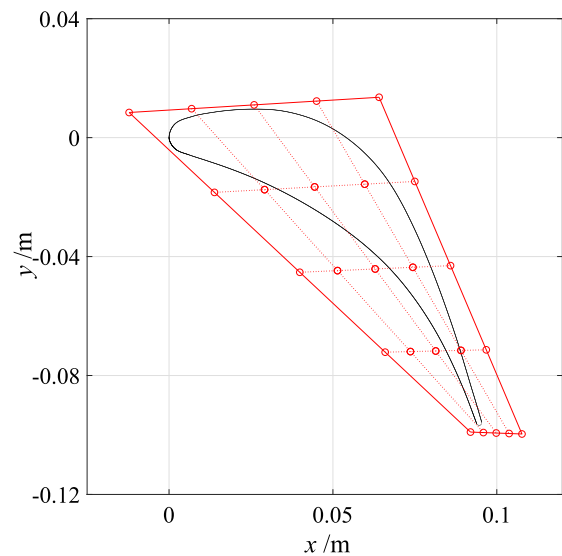


Fig. 24 White cascade: blade profile and FFD box control points

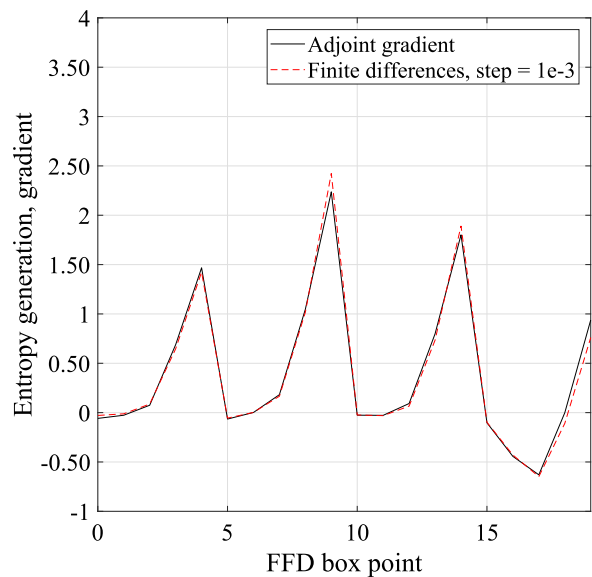


Fig. 25 White cascade: comparison between the entropy generation gradient calculated with the adjoint solver and the same quantity calculated with finite differences

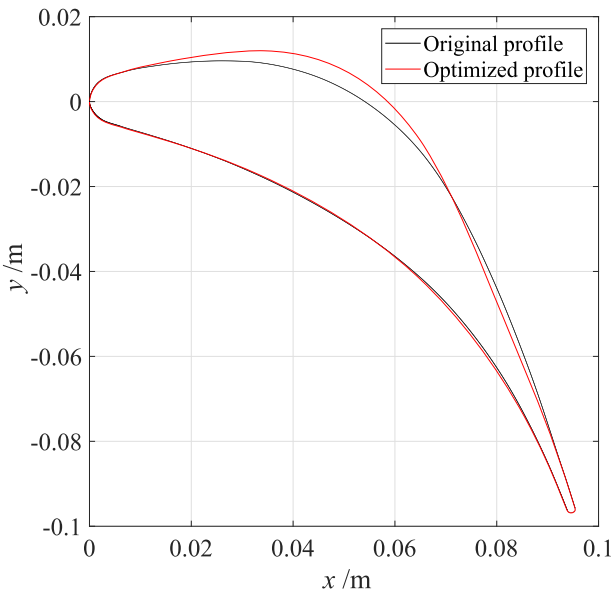


Fig. 26 White cascade: comparison between the original profile and the optimized profile in case the objective is the minimization of the liquid volume fraction

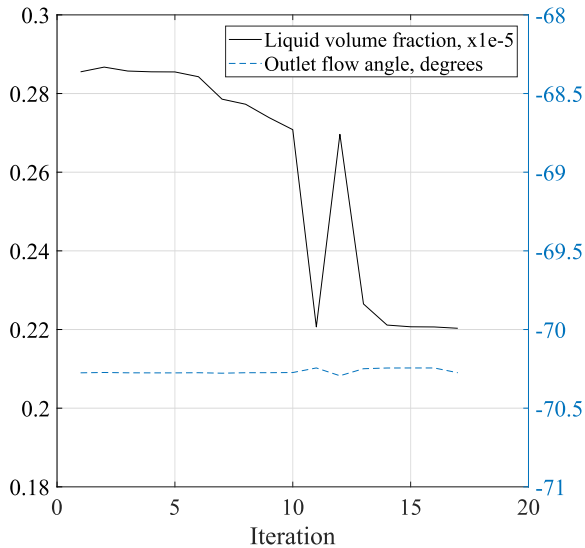


Fig. 27 White cascade: optimization history in case the objective is the minimization of the liquid volume fraction history

cascade. Therefore, the decrease of liquid volume fraction does not translate in a reduction of the loss coefficient $\zeta_{2\text{phase}}$.

Lastly, Figs. 31 and 32 show the optimal profile obtained when minimizing the entropy loss coefficient and the associated optimization history. Full convergence is achieved after four iterations, and the value of the objective function is reduced by about 12%, while the outlet flow angle remains practically unaltered.

The contours of the Mach number and the liquid volume fraction are instead displayed in Figs. 33 and 34. By comparison with the same contours of the baseline geometry of Figs. 22 and 23, it can be deduced that the optimization provides a geometry configuration that leads to lower Mach number flows and a shift of the condensation onset further downstream close to the blade trailing edge. As a consequence thereof, the flow reaches a lower degree of subcooling with positive impact in terms of wetness loss reduction. Differently from the Dykas cascade, the averaged liquid volume fraction also decreases by about 20%.

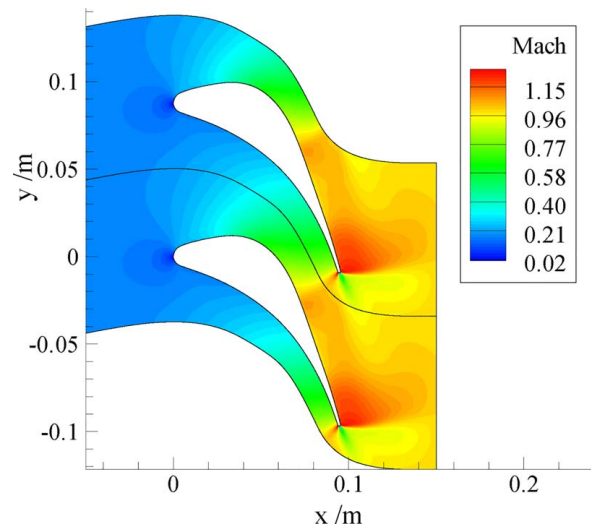


Fig. 28 White cascade: Mach number for the optimized profile in case the objective is the minimization of the liquid volume fraction

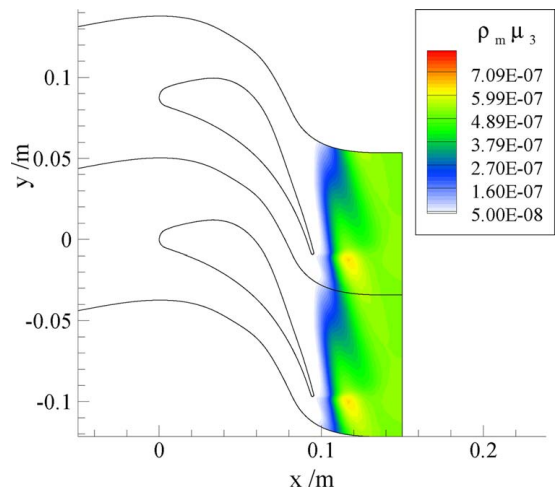


Fig. 29 White cascade: $U_{2\text{phase},4}$ for the optimized profile in case the objective is the minimization of the liquid volume fraction

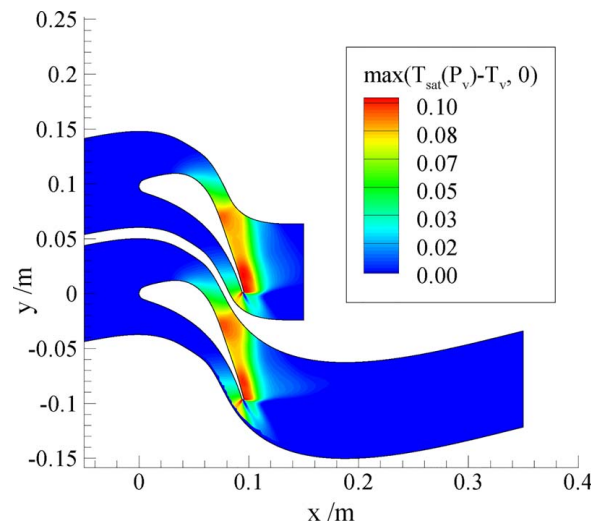


Fig. 30 White cascade: degree of subcooling ΔT_{sub} . Comparison between the simulations with the original domain (up) and the extended domain (down) using the optimized profile in case the objective is the minimization of the liquid volume fraction

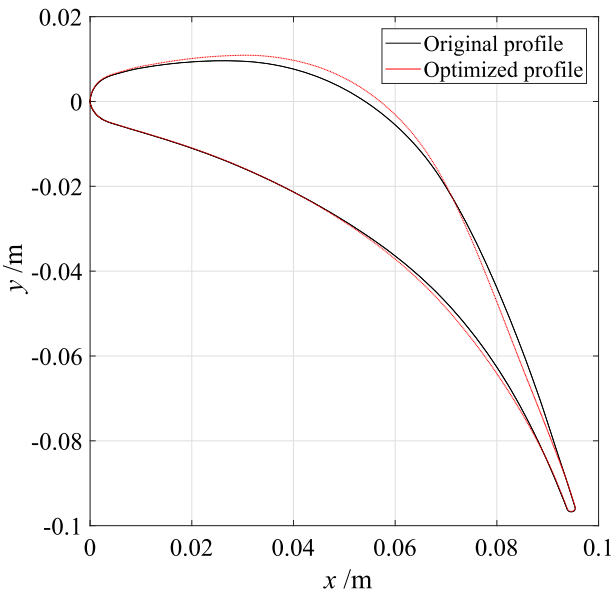


Fig. 31 White cascade: comparison between the original profile and the optimized profile in case the objective is the minimization of the thermodynamic losses

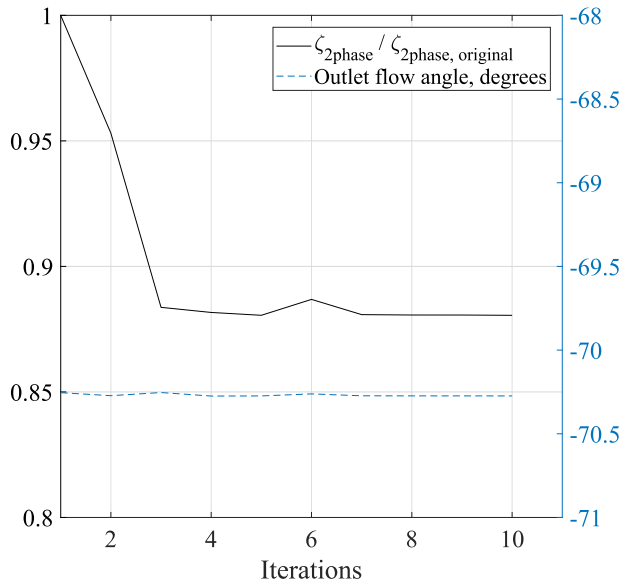


Fig. 32 White cascade: optimization history in case the objective is the minimization of the thermodynamic losses

Figure 35 reports the blade loading of the original and the optimized configuration, while Fig. 36 displays the degree of subcooling of the flow while passing through the cascade. The pressure distribution of the optimized cascade is obtained by using the two-phase and the single-phase model, namely, by assuming that no condensation is triggered when expanding the flow between the same conditions. The trends show that the pressure distribution around the optimal blade is comparatively equivalent in the two cases, suggesting that viscous dissipation on the blade walls is in turn mitigated by virtue of the removal of the condensation shock and of the velocity peak on the rear suction side. As can be observed in Fig. 36, the minimization of the thermodynamic losses eventually leads to a decrease of the degree of subcooling.

Ultimately, these results further corroborate the potential and the effectiveness of shape optimization for turbomachinery flow problems characterized by phase change.

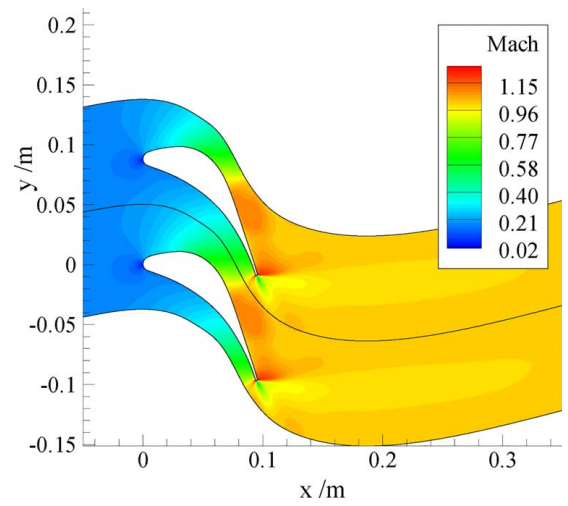


Fig. 33 White cascade: Mach number distribution for the optimized profile in case the objective is the minimization of the thermodynamic losses

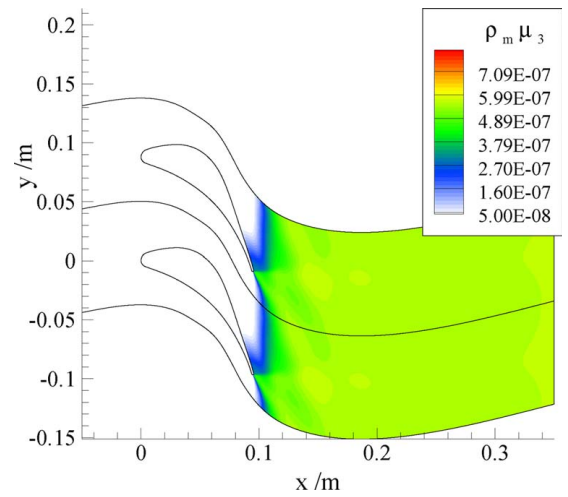


Fig. 34 White cascade: $U_{2\text{phase},4}$ distribution for the optimized profile in case the objective is the minimization of the thermodynamic losses

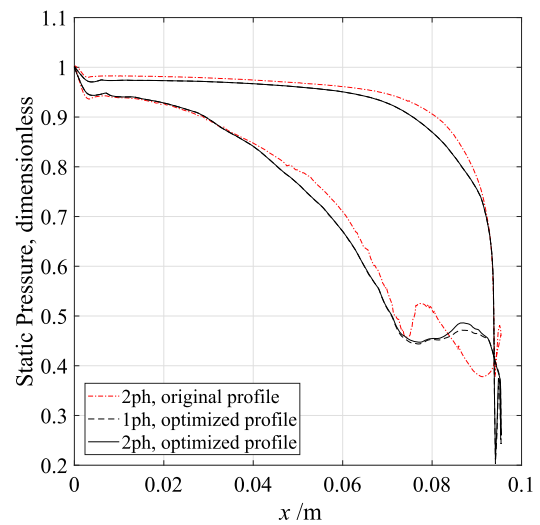


Fig. 35 White cascade: comparison between the blade loading of the baseline and that of the optimized configuration in case the objective is the minimization of the thermodynamic losses obtained by using both single- and two-phase simulations

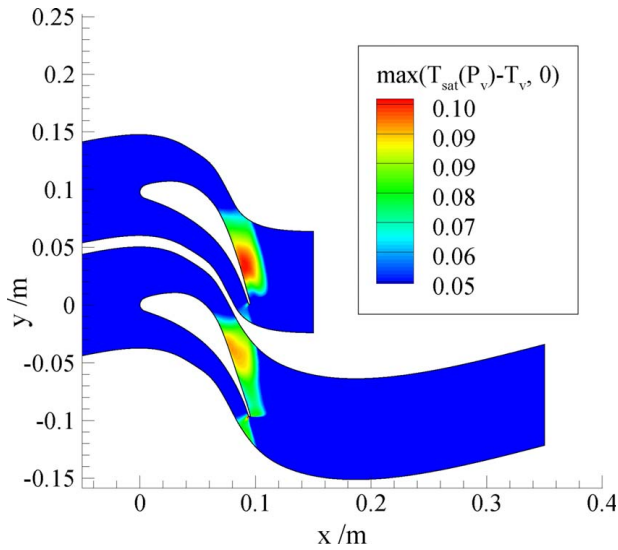


Fig. 36 White cascade: comparison between the degree of subcooling of the baseline (up) and that of the optimized configuration in case the objective is the minimization of the thermodynamic losses (down)

6 Conclusions

A fully turbulent adjoint-based optimization method for two-phase condensing flow problems in turbomachinery was developed and documented in this paper. The method was implemented in the open-source SU2 CFD software, which was extended to simulate metastable condensing flows by means of the method of moments. The adjoint solver is based on a duality-preserving algorithm, which enables the adjoint solver to inherit the same convergence properties of the primal flow solver. The optimization framework was then applied to the re-design of two turbine cascades representative of blade profiles adopted in steam turbines of large power capacity. The main outcomes of the study can be summarized as follows:

- (1) The adjoint solver is approximately two times computationally more expensive than the primal two-phase flow solver, while in terms of memory requirement the extra demand for the adjoint solver is of the order of three times. The computational performance is expected to scale similarly for three-dimensional cases.
- (2) For both cascade configurations, the adjoint-based constrained minimization of the liquid volume fraction led to abating the amount of condensate by nearly 24%, but at the expense of an increase of the entropy loss coefficient for the *Dykas cascade*.
- (3) The adjoint-based constrained minimization of the entropy coefficient allowed to considerably improve the simulated performance of both turbine cascades. In particular, the entropy loss coefficient reduced by 11% for the *Dykas cascade* and by 12% for the *White cascade*. The averaged liquid volume fraction at the outlet boundary obtained with the *Dykas cascade* turned out to be similar, while for the *White cascade*, it decreased by 20%. These observations suggest that the minimization of both objectives can be assured only by taking into account both objectives concurrently.

The development of an efficient fully turbulent adjoint optimization framework for two-phase flows and the demonstration of its capabilities for the re-design of steam turbine cascades paves the way for shape optimization of a number of turbomachinery applications characterized by phase change, such as supercritical CO₂

compressors, centrifugal compressors for refrigeration systems, and rocket engine turbo-pumps.

Acknowledgment

The authors would also like to thank T. Albring of TU Kaiserslautern for the very helpful discussions on the development of SU2 for two-phase flow applications entertained along the course of the work. The SU2 software used in this work can be downloaded at https://github.com/su2code/SU2/tree/feature_turbo2phase.

Data Availability Statement

The datasets generated and supporting the findings of this article are obtainable from the corresponding author upon reasonable request. The authors attest that all data for this study are included in the paper. Data provided by a third party are listed in Acknowledgments.

Nomenclature

Latin Letters

e	= internal energy
h	= enthalpy
k	= thermal conductivity
s	= entropy
t	= time
\mathbf{v}	= velocity
y	= liquid fraction
\mathbf{F}	= numerical flux
G	= growth rate
\mathcal{G}	= generic function to calculate the system solution
I	= turbulence intensity
J	= nucleation rate
\mathcal{J}	= objective function
L	= lagrangian function
\mathbf{M}	= function for the mesh deformation algorithm
N	= droplets number
\mathcal{N}	= generic function for fixed point iteration algorithm
P	= pressure
\mathbf{P}	= generic inverse matrix
\mathbf{Q}	= vector of the source terms
R	= average radius
\mathcal{R}	= gas constant
\mathbf{R}	= residual vector
S	= source term
T	= temperature
\mathbf{U}	= vector of the conservative variables
\mathbf{X}	= vector of grid points in the domain
\dot{m}	= mass flowrate
k_b	= Boltzmann constant
R_*	= critical radius
MM	= molecular mass
Pr	= Prandtl number

Greek Symbols

α	= averaged outlet flow angle
$\boldsymbol{\alpha}$	= vector of the design variables
γ	= heat capacity ratio
$\Delta\mathcal{G}$	= Gibbs free energy variation
$\Delta\dot{s}$	= entropy generation per unit of mass
ΔT_{sub}	= degree of subcooling
ζ	= loss coefficient
λ	= lagrangian multiplier
μ	= viscosity
μ_j	= generic moment of order $-j$
$\boldsymbol{\mu}$	= lagrangian multiplier

ρ = density
 σ = surface tension
 τ = viscous tensor

Subscripts

0 = total property
 2phase = term of the two-phase equations
 b = baseline case
 flow = term of the flow equations
 in = inlet quantity
 l = property of the liquid phase
 m = property of the two-phase mixture
 mass = mass quantity
 out = outlet quantity
 s = static property
 SA = term related to the turbulence model SA
 sat = saturation conditions
 turb = term of the turbulent equations
 v = property of the vapor phase
 vol = volumetric quantity
 x = component along the x -axis
 y = component along the y -axis

Superscripts

c = convective flux
 n = solution at time n
 v = viscous flux

Appendix

Closure Models. The critical radius R_* is evaluated as

$$R_* = \frac{2\sigma}{\rho_l \Delta \mathcal{G}} \quad (\text{A1})$$

in which σ is the surface tension, ρ_l is the liquid density, and $\Delta \mathcal{G}$ is the Gibbs free energy variation of the vapor phase.

The nucleation rate J is calculated as

$$J = \frac{1}{1 + \theta} \frac{\rho_v}{\rho_l} \sqrt{\frac{2\sigma}{\pi MM^3}} \exp\left(-\frac{4\pi R_*^2 \sigma}{3k_b T_v}\right) \quad (\text{A2})$$

in which

$$\theta = 2 \frac{\gamma - 1}{\gamma + 1} \frac{h_v - h_l}{\mathcal{R} T_v} \left(\frac{h_v - h_l}{\mathcal{R} T_v} - 0.5 \right) \quad (\text{A3})$$

σ is the surface tension, MM is the molecular mass, k_b is the Boltzmann constant, $\rho_{v,1}$ and $h_{v,1}$ are the densities and the specific enthalpies of the vapor and the liquid phase, respectively, γ is the heat

Table 4 Blade surface coordinates of the original White cascade

Pressure side		Suction side	
x	y	x	y
0.00000	0.00000	0.09741	-0.09000
0.00022	-0.00057	0.09505	-0.08400
0.00262	-0.00378	0.08889	-0.06340
0.00733	-0.00654	0.08348	-0.04735
0.01632	-0.00997	0.07751	-0.03222
0.02564	-0.01318	0.07196	-0.02075
0.03463	-0.01731	0.06324	-0.00780
0.04296	-0.02201	0.05395	0.00069
0.05128	-0.02729	0.04343	0.00619
0.05970	-0.03382	0.03201	0.00860
0.06681	-0.04070	0.02213	0.00848
0.07337	-0.04815	0.01190	0.00688
0.07893	-0.05572	0.00486	0.00482
0.08460	-0.06478	0.00255	0.00378
0.08884	-0.07372	0.00034	0.00183
0.09285	-0.08335	0.00000	0.00000
0.09410	-0.08713		
0.09618	-0.09250		
0.09741	-0.09401		
0.09785	-0.09400		

capacity ratio, and \mathcal{R} is the gas constant. The growth rate G is

$$G = \frac{\kappa_v (T_{\text{sat}}(P_v) - T_v) (1 - (R_*/R))}{\rho_l (h_v - h_l) (1.89 + R - 1.89\nu(\lambda_v/Pr))} \quad (\text{A4})$$

in which Pr is the Prandtl number, λ_v is given by

$$\lambda_v = \frac{1.5\mu_v \sqrt{\mathcal{R} T_v}}{P_v} \quad (\text{A5})$$

κ_v and μ_v are the thermal conductivity and viscosity of the vapor phase, respectively, and ν is defined as

$$\nu = \frac{\mathcal{R} T_{\text{sat}}(P_v)}{h_v - h_l} \left[0.5 - \frac{1}{4} \frac{\gamma + 1}{\gamma - 1} \frac{\mathcal{R} T_{\text{sat}}(P_v)}{h_v - h_l} \right] \quad (\text{A6})$$

The capillarity model adopted for the liquid phase temperature T_l is [34,35]

$$T_l = T_{\text{sat}}(P) - (T_{\text{sat}}(P) - T_v) \frac{R_*}{R} \quad (\text{A7})$$

where $T_{\text{sat}}(P)$ is the saturation temperature at the vapor pressure P , T_v is the vapor temperature, R is the droplets average radius, and R_* is the critical radius.

Blade Profiles. Tables 4–8 report the following, respectively,

- (1) The blade profile for the cascade in Ref. [33].

Table 5 Blade surface coordinates of the optimized profile of the Dykas cascade

Point #	x	y	Point #	x	y	Point #	x	y
1	2.267×10^{-03}	2.959×10^{-03}	37	1.476×10^{-01}	-6.947×10^{-02}	73	4.373×10^{-03}	-1.629×10^{-02}
2	6.199×10^{-03}	8.055×10^{-03}	38	1.499×10^{-01}	-7.443×10^{-02}	74	1.124×10^{-03}	-1.244×10^{-02}
3	1.092×10^{-02}	1.145×10^{-02}	39	1.521×10^{-01}	-7.940×10^{-02}	75	1.000×10^{-07}	-6.199×10^{-03}
4	1.570×10^{-02}	1.439×10^{-02}	40	1.543×10^{-01}	-8.439×10^{-02}	76	1.328×10^{-03}	8.031×10^{-04}
5	2.054×10^{-02}	1.692×10^{-02}	41	1.564×10^{-01}	-8.936×10^{-02}	77	1.729×10^{-01}	-1.429×10^{-01}
6	2.544×10^{-02}	1.905×10^{-02}	42	1.416×10^{-01}	-8.474×10^{-02}	78	1.722×10^{-01}	-1.409×10^{-01}
7	3.039×10^{-02}	2.082×10^{-02}	43	1.383×10^{-01}	-8.041×10^{-02}	79	1.714×10^{-01}	-1.389×10^{-01}
8	3.539×10^{-02}	2.223×10^{-02}	44	1.349×10^{-01}	-7.611×10^{-02}	80	1.707×10^{-01}	-1.370×10^{-01}
9	4.043×10^{-02}	2.333×10^{-02}	45	1.315×10^{-01}	-7.189×10^{-02}	81	1.699×10^{-01}	-1.350×10^{-01}
10	4.552×10^{-02}	2.406×10^{-02}	46	1.279×10^{-01}	-6.774×10^{-02}	82	1.691×10^{-01}	-1.330×10^{-01}
11	5.066×10^{-02}	2.430×10^{-02}	47	1.243×10^{-01}	-6.366×10^{-02}	83	1.672×10^{-01}	-1.286×10^{-01}
12	5.583×10^{-02}	2.409×10^{-02}	48	1.206×10^{-01}	-5.965×10^{-02}	84	1.650×10^{-01}	-1.238×10^{-01}
13	6.101×10^{-02}	2.343×10^{-02}	49	1.168×10^{-01}	-5.573×10^{-02}	85	1.627×10^{-01}	-1.191×10^{-01}
14	6.617×10^{-02}	2.235×10^{-02}	50	1.129×10^{-01}	-5.190×10^{-02}	86	1.603×10^{-01}	-1.144×10^{-01}
15	7.128×10^{-02}	2.088×10^{-02}	51	1.089×10^{-01}	-4.817×10^{-02}	87	1.577×10^{-01}	-1.098×10^{-01}
16	7.631×10^{-02}	1.901×10^{-02}	52	1.048×10^{-01}	-4.448×10^{-02}	88	1.551×10^{-01}	-1.052×10^{-01}
17	8.125×10^{-02}	1.679×10^{-02}	53	1.007×10^{-01}	-4.094×10^{-02}	89	1.523×10^{-01}	-1.006×10^{-01}
18	8.606×10^{-02}	1.422×10^{-02}	54	9.646×10^{-02}	-3.757×10^{-02}	90	1.494×10^{-01}	-9.610×10^{-02}
19	9.074×10^{-02}	1.135×10^{-02}	55	9.211×10^{-02}	-3.437×10^{-02}	91	1.464×10^{-01}	-9.161×10^{-02}
20	9.529×10^{-02}	8.205×10^{-03}	56	8.767×10^{-02}	-3.135×10^{-02}	92	1.433×10^{-01}	-8.717×10^{-02}
21	9.969×10^{-02}	4.802×10^{-03}	57	8.315×10^{-02}	-2.852×10^{-02}	93	1.594×10^{-01}	-9.646×10^{-02}
22	1.039×10^{-01}	1.139×10^{-03}	58	7.855×10^{-02}	-2.589×10^{-02}	94	1.613×10^{-01}	-1.013×10^{-01}
23	1.080×10^{-01}	-2.770×10^{-03}	59	7.387×10^{-02}	-2.346×10^{-02}	95	1.632×10^{-01}	-1.061×10^{-01}
24	1.118×10^{-01}	-6.910×10^{-03}	60	6.912×10^{-02}	-2.125×10^{-02}	96	1.650×10^{-01}	-1.109×10^{-01}
25	1.155×10^{-01}	-1.125×10^{-02}	61	6.430×10^{-02}	-1.925×10^{-02}	97	1.667×10^{-01}	-1.156×10^{-01}
26	1.188×10^{-01}	-1.577×10^{-02}	62	5.943×10^{-02}	-1.750×10^{-02}	98	1.683×10^{-01}	-1.203×10^{-01}
27	1.219×10^{-01}	-2.045×10^{-02}	63	5.451×10^{-02}	-1.599×10^{-02}	99	1.699×10^{-01}	-1.250×10^{-01}
28	1.248×10^{-01}	-2.524×10^{-02}	64	4.954×10^{-02}	-1.476×10^{-02}	100	1.714×10^{-01}	-1.297×10^{-01}
29	1.276×10^{-01}	-3.012×10^{-02}	65	4.453×10^{-02}	-1.382×10^{-02}	101	1.726×10^{-01}	-1.336×10^{-01}
30	1.302×10^{-01}	-3.501×10^{-02}	66	3.950×10^{-02}	-1.319×10^{-02}	102	1.731×10^{-01}	-1.355×10^{-01}
31	1.329×10^{-01}	-3.990×10^{-02}	67	3.444×10^{-02}	-1.289×10^{-02}	103	1.737×10^{-01}	-1.373×10^{-01}
32	1.355×10^{-01}	-4.480×10^{-02}	68	2.936×10^{-02}	-1.295×10^{-02}	104	1.742×10^{-01}	-1.391×10^{-01}
33	1.380×10^{-01}	-4.971×10^{-02}	69	2.428×10^{-02}	-1.339×10^{-02}	105	1.747×10^{-01}	-1.410×10^{-01}
34	1.405×10^{-01}	-5.464×10^{-02}	70	1.918×10^{-02}	-1.425×10^{-02}	106	1.751×10^{-01}	-1.428×10^{-01}
35	1.429×10^{-01}	-5.958×10^{-02}	71	1.409×10^{-02}	-1.555×10^{-02}			
36	1.453×10^{-01}	-6.452×10^{-02}	72	9.020×10^{-03}	-1.703×10^{-02}			

Note: Cost function: liquid volume fraction.

Table 6 Blade surface coordinates of the optimized profile of the Dykas cascade

Point #	x	y	Point #	x	y	Point #	x	y
1	8.610×10^{-05}	6.141×10^{-04}	37	6.160×10^{-02}	-1.893×10^{-02}	73	1.471×10^{-01}	-6.853×10^{-02}
2	1.931×10^{-03}	5.614×10^{-03}	38	1.084×10^{-01}	-8.007×10^{-03}	74	1.479×10^{-01}	-7.029×10^{-02}
3	1.041×10^{-04}	-2.373×10^{-03}	39	6.591×10^{-02}	-2.070×10^{-02}	75	1.507×10^{-01}	-1.039×10^{-01}
4	8.811×10^{-03}	1.053×10^{-02}	40	7.124×10^{-02}	-2.315×10^{-02}	76	1.523×10^{-01}	-1.064×10^{-01}
5	1.463×10^{-02}	1.278×10^{-02}	41	1.106×10^{-01}	-1.004×10^{-02}	77	1.514×10^{-01}	-7.869×10^{-02}
6	5.211×10^{-03}	8.827×10^{-03}	42	7.751×10^{-02}	-2.645×10^{-02}	78	1.551×10^{-01}	-1.110×10^{-01}
7	1.839×10^{-02}	1.405×10^{-02}	43	8.112×10^{-02}	-2.855×10^{-02}	79	1.566×10^{-01}	-1.136×10^{-01}
8	2.271×10^{-02}	1.534×10^{-02}	44	1.151×10^{-01}	-1.466×10^{-02}	80	1.543×10^{-01}	-8.613×10^{-02}
9	2.764×10^{-02}	1.659×10^{-02}	45	8.817×10^{-02}	-3.312×10^{-02}	81	1.548×10^{-01}	-8.739×10^{-02}
10	2.984×10^{-02}	1.708×10^{-02}	46	9.114×10^{-02}	-3.524×10^{-02}	82	1.606×10^{-01}	-1.204×10^{-01}
11	3.987×10^{-02}	1.872×10^{-02}	47	9.357×10^{-02}	-3.707×10^{-02}	83	1.627×10^{-01}	-1.242×10^{-01}
12	3.539×10^{-02}	1.810×10^{-02}	48	9.550×10^{-02}	-3.858×10^{-02}	84	1.640×10^{-01}	-1.264×10^{-01}
13	4.382×10^{-02}	1.910×10^{-02}	49	1.195×10^{-01}	-1.988×10^{-02}	85	1.589×10^{-01}	-9.870×10^{-02}
14	4.834×10^{-03}	-9.860×10^{-03}	50	1.016×10^{-01}	-4.375×10^{-02}	86	1.660×10^{-01}	-1.300×10^{-01}
15	5.066×10^{-02}	1.919×10^{-02}	51	1.039×10^{-01}	-4.583×10^{-02}	87	1.605×10^{-01}	-1.030×10^{-01}
16	5.526×10^{-02}	1.885×10^{-02}	52	1.066×10^{-01}	-4.843×10^{-02}	88	1.615×10^{-01}	-1.061×10^{-01}
17	5.698×10^{-02}	1.864×10^{-02}	53	1.232×10^{-01}	-2.491×10^{-02}	89	1.690×10^{-01}	-1.353×10^{-01}
18	6.388×10^{-02}	1.737×10^{-02}	54	1.129×10^{-01}	-5.463×10^{-02}	90	1.692×10^{-01}	-1.358×10^{-01}
19	6.788×10^{-02}	1.631×10^{-02}	55	1.150×10^{-01}	-5.690×10^{-02}	91	1.695×10^{-01}	-1.364×10^{-01}
20	7.296×10^{-02}	1.461×10^{-02}	56	1.193×10^{-01}	-6.153×10^{-02}	92	1.708×10^{-01}	-1.390×10^{-01}
21	7.520×10^{-02}	1.374×10^{-02}	57	1.273×10^{-01}	-3.109×10^{-02}	93	1.709×10^{-01}	-1.391×10^{-01}
22	7.797×10^{-02}	1.256×10^{-02}	58	1.206×10^{-01}	-6.296×10^{-02}	94	1.713×10^{-01}	-1.398×10^{-01}
23	8.179×10^{-02}	1.074×10^{-02}	59	1.299×10^{-01}	-3.548×10^{-02}	95	1.722×10^{-01}	-1.417×10^{-01}
24	1.692×10^{-02}	-1.102×10^{-02}	60	1.259×10^{-01}	-6.922×10^{-02}	96	1.727×10^{-01}	-1.430×10^{-01}
25	1.975×10^{-02}	-1.099×10^{-02}	61	1.326×10^{-01}	-3.995×10^{-02}	97	1.672×10^{-01}	-1.224×10^{-01}
26	9.074×10^{-02}	5.602×10^{-03}	62	1.335×10^{-01}	-4.145×10^{-02}	98	1.737×10^{-01}	-1.441×10^{-01}
27	2.428×10^{-02}	-1.109×10^{-02}	63	1.311×10^{-01}	-7.562×10^{-02}	99	1.742×10^{-01}	-1.441×10^{-01}
28	2.710×10^{-02}	-1.125×10^{-02}	64	1.363×10^{-01}	-4.656×10^{-02}	100	1.709×10^{-01}	-1.321×10^{-01}
29	3.162×10^{-02}	-1.164×10^{-02}	65	1.334×10^{-01}	-7.864×10^{-02}	101	1.750×10^{-01}	-1.436×10^{-01}
30	3.500×10^{-02}	-1.205×10^{-02}	66	1.391×10^{-01}	-5.181×10^{-02}	102	1.751×10^{-01}	-1.431×10^{-01}
31	1.016×10^{-01}	-2.156×10^{-03}	67	1.383×10^{-01}	-8.525×10^{-02}	103	1.729×10^{-01}	-1.374×10^{-01}
32	1.011×10^{-01}	-1.780×10^{-03}	68	1.397×10^{-01}	-8.730×10^{-02}	104	1.734×10^{-01}	-1.386×10^{-01}
33	4.565×10^{-02}	-1.401×10^{-02}	69	1.416×10^{-01}	-8.987×10^{-02}	105	1.740×10^{-01}	-1.400×10^{-01}
34	1.025×10^{-01}	-2.911×10^{-03}	70	1.440×10^{-01}	-9.349×10^{-02}	106	1.741×10^{-01}	-1.404×10^{-01}
35	1.044×10^{-01}	-4.448×10^{-03}	71	1.443×10^{-01}	-6.223×10^{-02}			
36	5.560×10^{-02}	-1.679×10^{-02}	72	1.461×10^{-01}	-9.660×10^{-02}			

Note: Cost function: thermodynamic losses.

Table 7 Blade surface coordinates of the optimized profile of the White cascade

Point #	x	y	Point #	x	y	Point #	x	y
1	2.80×10^{-05}	-6.09×10^{-04}	38	8.37×10^{-02}	-7.06×10^{-02}	75	7.94×10^{-02}	-4.53×10^{-02}
2	1.04×10^{-03}	-3.03×10^{-03}	39	8.51×10^{-02}	-7.34×10^{-02}	76	7.83×10^{-02}	-4.22×10^{-02}
3	3.22×10^{-03}	-4.89×10^{-03}	40	8.63×10^{-02}	-7.62×10^{-02}	77	7.72×10^{-02}	-3.91×10^{-02}
4	5.96×10^{-03}	-5.93×10^{-03}	41	8.76×10^{-02}	-7.90×10^{-02}	78	7.61×10^{-02}	-3.58×10^{-02}
5	8.73×10^{-03}	-6.93×10^{-03}	42	8.88×10^{-02}	-8.19×10^{-02}	79	7.49×10^{-02}	-3.25×10^{-02}
6	1.15×10^{-02}	-7.89×10^{-03}	43	8.99×10^{-02}	-8.49×10^{-02}	80	7.37×10^{-02}	-2.91×10^{-02}
7	1.43×10^{-02}	-8.88×10^{-03}	44	9.10×10^{-02}	-8.79×10^{-02}	81	7.24×10^{-02}	-2.56×10^{-02}
8	1.71×10^{-02}	-9.90×10^{-03}	45	9.21×10^{-02}	-9.10×10^{-02}	82	7.11×10^{-02}	-2.22×10^{-02}
9	1.98×10^{-02}	-1.10×10^{-02}	46	9.31×10^{-02}	-9.41×10^{-02}	83	6.96×10^{-02}	-1.87×10^{-02}
10	2.26×10^{-02}	-1.21×10^{-02}	47	9.36×10^{-02}	-9.54×10^{-02}	84	6.81×10^{-02}	-1.53×10^{-02}
11	2.53×10^{-02}	-1.33×10^{-02}	48	9.38×10^{-02}	-9.61×10^{-02}	85	6.65×10^{-02}	-1.19×10^{-02}
12	2.80×10^{-02}	-1.45×10^{-02}	49	9.41×10^{-02}	-9.67×10^{-02}	86	6.47×10^{-02}	-8.69×10^{-03}
13	3.07×10^{-02}	-1.59×10^{-02}	50	9.48×10^{-02}	-9.68×10^{-02}	87	6.28×10^{-02}	-5.64×10^{-03}
14	3.33×10^{-02}	-1.72×10^{-02}	51	9.53×10^{-02}	-9.64×10^{-02}	88	6.08×10^{-02}	-2.79×10^{-03}
15	3.60×10^{-02}	-1.87×10^{-02}	52	9.54×10^{-02}	-9.58×10^{-02}	89	5.87×10^{-02}	-1.68×10^{-04}
16	3.86×10^{-02}	-2.02×10^{-02}	53	9.52×10^{-02}	-9.52×10^{-02}	90	5.64×10^{-02}	2.24×10^{-03}
17	4.11×10^{-02}	-2.18×10^{-02}	54	9.51×10^{-02}	-9.46×10^{-02}	91	5.41×10^{-02}	4.40×10^{-03}
18	4.37×10^{-02}	-2.35×10^{-02}	55	9.49×10^{-02}	-9.40×10^{-02}	92	5.16×10^{-02}	6.30×10^{-03}
19	4.62×10^{-02}	-2.52×10^{-02}	56	9.47×10^{-02}	-9.33×10^{-02}	93	4.91×10^{-02}	9.92×10^{-03}
20	4.87×10^{-02}	-2.70×10^{-02}	57	9.46×10^{-02}	-9.27×10^{-02}	94	4.65×10^{-02}	9.27×10^{-03}
21	5.12×10^{-02}	-2.88×10^{-02}	58	9.43×10^{-02}	-9.18×10^{-02}	95	4.37×10^{-02}	1.03×10^{-02}
22	5.36×10^{-02}	-3.08×10^{-02}	59	9.36×10^{-02}	-8.91×10^{-02}	96	4.09×10^{-02}	1.11×10^{-02}
23	5.59×10^{-02}	-3.28×10^{-02}	60	9.28×10^{-02}	-8.64×10^{-02}	97	3.81×10^{-02}	1.16×10^{-02}
24	5.83×10^{-02}	-3.49×10^{-02}	61	9.21×10^{-02}	-8.37×10^{-02}	98	3.52×10^{-02}	1.19×10^{-02}
25	6.05×10^{-02}	-3.71×10^{-02}	62	9.13×10^{-02}	-8.12×10^{-02}	99	3.22×10^{-02}	1.20×10^{-02}
26	6.27×10^{-02}	-3.94×10^{-02}	63	9.06×10^{-02}	-7.87×10^{-02}	100	2.93×10^{-02}	1.18×10^{-02}
27	6.49×10^{-02}	-4.17×10^{-02}	64	8.99×10^{-02}	-7.63×10^{-02}	101	2.63×10^{-02}	1.14×10^{-02}
28	6.70×10^{-02}	-4.42×10^{-02}	65	8.91×10^{-02}	-7.39×10^{-02}	102	2.34×10^{-02}	1.10×10^{-02}
29	6.89×10^{-02}	-4.66×10^{-02}	66	8.83×10^{-02}	-7.15×10^{-02}	103	2.05×10^{-02}	1.05×10^{-02}
30	7.09×10^{-02}	-4.92×10^{-02}	67	8.76×10^{-02}	-6.91×10^{-02}	104	1.76×10^{-02}	9.93×10^{-03}
31	7.27×10^{-02}	-5.18×10^{-02}	68	8.68×10^{-02}	-6.68×10^{-02}	105	1.47×10^{-02}	9.28×10^{-03}
32	7.45×10^{-02}	-5.44×10^{-02}	69	8.59×10^{-02}	-6.44×10^{-02}	106	1.18×10^{-02}	8.57×10^{-03}
33	7.62×10^{-02}	-5.71×10^{-02}	70	8.51×10^{-02}	-6.19×10^{-02}	107	9.00×10^{-03}	7.82×10^{-03}
34	7.78×10^{-02}	-5.97×10^{-02}	71	8.42×10^{-02}	-5.93×10^{-02}	108	6.23×10^{-03}	6.84×10^{-03}
35	7.94×10^{-02}	-6.24×10^{-02}	72	8.33×10^{-02}	-5.67×10^{-02}	109	3.53×10^{-03}	5.75×10^{-03}
36	8.09×10^{-02}	-6.51×10^{-02}	73	8.23×10^{-02}	-5.40×10^{-02}	110	1.33×10^{-03}	3.88×10^{-03}
37	8.24×10^{-02}	-6.79×10^{-02}	74	8.14×10^{-02}	-5.12×10^{-02}	111	1.78×10^{-04}	1.25×10^{-03}

Note: Cost function: liquid volume fraction.

Table 8 Blade surface coordinates of the optimized profile of the White cascade

Point #	x	y	Point #	x	y	Point #	x	y
1	3.51×10^{-03}	-4.78×10^{-03}	38	7.47×10^{-02}	-3.18×10^{-02}	75	8.66×10^{-02}	-7.71×10^{-02}
2	1.23×10^{-03}	-3.03×10^{-03}	39	7.59×10^{-02}	-3.52×10^{-02}	76	8.54×10^{-02}	-7.44×10^{-02}
3	2.80×10^{-05}	-3.42×10^{-04}	40	7.71×10^{-02}	-3.85×10^{-02}	77	8.41×10^{-02}	-7.18×10^{-02}
4	5.61×10^{-04}	2.75×10^{-03}	41	7.82×10^{-02}	-4.18×10^{-02}	78	8.27×10^{-02}	-6.91×10^{-02}
5	2.18×10^{-03}	5.12×10^{-03}	42	7.93×10^{-02}	-4.50×10^{-02}	79	8.13×10^{-02}	-6.64×10^{-02}
6	4.69×10^{-03}	6.53×10^{-03}	43	8.03×10^{-02}	-4.82×10^{-02}	80	7.98×10^{-02}	-6.37×10^{-02}
7	7.44×10^{-03}	7.51×10^{-03}	44	8.13×10^{-02}	-5.13×10^{-02}	81	7.82×10^{-02}	-6.11×10^{-02}
8	1.02×10^{-02}	8.31×10^{-03}	45	8.23×10^{-02}	-5.43×10^{-02}	82	7.66×10^{-02}	-5.84×10^{-02}
9	1.31×10^{-02}	8.93×10^{-03}	46	8.32×10^{-02}	-5.72×10^{-02}	83	7.49×10^{-02}	-5.57×10^{-02}
10	1.60×10^{-02}	9.49×10^{-03}	47	8.42×10^{-02}	-6.01×10^{-02}	84	7.31×10^{-02}	-5.31×10^{-02}
11	1.88×10^{-02}	9.97×10^{-03}	48	8.51×10^{-02}	-6.28×10^{-02}	85	7.13×10^{-02}	-5.04×10^{-02}
12	2.18×10^{-02}	1.03×10^{-02}	49	8.59×10^{-02}	-6.55×10^{-02}	86	6.94×10^{-02}	-4.79×10^{-02}
13	2.47×10^{-02}	1.06×10^{-02}	50	8.68×10^{-02}	-6.81×10^{-02}	87	6.74×10^{-02}	-4.54×10^{-02}
14	2.76×10^{-02}	1.08×10^{-02}	51	8.76×10^{-02}	-7.06×10^{-02}	88	6.54×10^{-02}	-4.29×10^{-02}
15	3.05×10^{-02}	1.09×10^{-02}	52	8.85×10^{-02}	-7.30×10^{-02}	89	6.32×10^{-02}	-4.05×10^{-02}
16	3.35×10^{-02}	1.08×10^{-02}	53	8.92×10^{-02}	-7.54×10^{-02}	90	6.10×10^{-02}	-3.82×10^{-02}
17	3.64×10^{-02}	1.04×10^{-02}	54	9.00×10^{-02}	-7.77×10^{-02}	91	5.88×10^{-02}	-3.60×10^{-02}
18	3.93×10^{-02}	9.88×10^{-03}	55	9.08×10^{-02}	-8.00×10^{-02}	92	5.65×10^{-02}	-3.38×10^{-02}
19	4.21×10^{-02}	9.11×10^{-03}	56	9.15×10^{-02}	-8.23×10^{-02}	93	5.41×10^{-02}	-3.17×10^{-02}
20	4.49×10^{-02}	8.12×10^{-03}	57	9.23×10^{-02}	-8.47×10^{-02}	94	5.17×10^{-02}	-2.98×10^{-02}
21	4.76×10^{-02}	6.89×10^{-03}	58	9.30×10^{-02}	-8.71×10^{-02}	95	4.93×10^{-02}	-2.78×10^{-02}
22	5.02×10^{-02}	5.42×10^{-03}	59	9.38×10^{-02}	-8.96×10^{-02}	96	4.68×10^{-02}	-2.60×10^{-02}
23	5.27×10^{-02}	3.73×10^{-03}	60	9.45×10^{-02}	-9.22×10^{-02}	97	4.43×10^{-02}	-2.42×10^{-02}
24	5.51×10^{-02}	1.81×10^{-03}	61	9.52×10^{-02}	-9.49×10^{-02}	98	4.17×10^{-02}	-2.25×10^{-02}
25	5.74×10^{-02}	-3.06×10^{-04}	62	9.54×10^{-02}	-9.55×10^{-02}	99	3.92×10^{-02}	-2.08×10^{-02}
26	5.96×10^{-02}	-2.63×10^{-03}	63	9.54×10^{-02}	-9.58×10^{-02}	100	3.66×10^{-02}	-1.92×10^{-02}
27	6.17×10^{-02}	-5.14×10^{-03}	64	9.53×10^{-02}	-9.62×10^{-02}	101	3.39×10^{-02}	-1.77×10^{-02}
28	6.36×10^{-02}	-7.84×10^{-03}	65	9.51×10^{-02}	-9.64×10^{-02}	102	3.13×10^{-02}	-1.63×10^{-02}
29	6.55×10^{-02}	-1.07×10^{-02}	66	9.48×10^{-02}	-9.66×10^{-02}	103	2.86×10^{-02}	-1.49×10^{-02}
30	6.72×10^{-02}	-1.38×10^{-02}	67	9.45×10^{-02}	-9.66×10^{-02}	104	2.59×10^{-02}	-1.36×10^{-02}
31	6.87×10^{-02}	-1.70×10^{-02}	68	9.42×10^{-02}	-9.65×10^{-02}	105	2.32×10^{-02}	-1.23×10^{-02}
32	7.02×10^{-02}	-2.02×10^{-02}	69	9.39×10^{-02}	-9.62×10^{-02}	106	2.05×10^{-02}	-1.11×10^{-02}
33	7.16×10^{-02}	-2.36×10^{-02}	70	9.38×10^{-02}	-9.58×10^{-02}	107	1.77×10^{-02}	-1.00×10^{-02}
34	7.29×10^{-02}	-2.69×10^{-02}	71	9.12×10^{-02}	-8.82×10^{-02}	108	1.49×10^{-02}	-8.94×10^{-03}
35	9.38×10^{-02}	-9.58×10^{-02}	72	9.02×10^{-02}	-8.53×10^{-02}	109	1.21×10^{-02}	-7.92×10^{-03}
36	9.28×10^{-02}	-9.26×10^{-02}	73	8.90×10^{-02}	-8.25×10^{-02}	110	9.35×10^{-03}	-6.92×10^{-03}
37	7.35×10^{-02}	-2.84×10^{-02}	74	8.78×10^{-02}	-7.98×10^{-02}	111	6.57×10^{-03}	-5.92×10^{-03}

Note: Cost function: thermodynamic losses.

- (2) The optimized profile for minimum volume liquid fraction for the cascade [32].
- (3) The optimized profile for minimum losses for the cascade [32].
- (4) The optimized profile for minimum volume liquid fraction for the cascade [33].
- (5) The optimized profile for minimum losses for the cascade [33].

All coordinates are in meters.

References

- [1] Jameson, A., 1988, "Aerodynamic Design Via Control Theory," *J. Sci. Comput.*, **3**(3), pp. 233–260.
- [2] Jameson, A., Martinelli, L., and Pierce, N. A., 1998, "Optimum Aerodynamic Design Using the Navier–Stokes Equations," *Theor. Comput. Fluid Dyn.*, **10**(1), pp. 213–237.
- [3] Reuther, J. J., Jameson, A., Alonso, J. J., Rimlinger, M. J., and Saunders, D., 1999, "Constrained Multipoint Aerodynamic Shape Optimization Using An Adjoint Formulation and Parallel Computers, Part 1," *J. Aircraft*, **36**(1), pp. 51–60.
- [4] Mader, C. A., Alonso, J. J., and Der Weide, E. V., 2008, "Adjoint: An Approach for the Rapid Development of Discrete Adjoint Solvers," *AIAA J.*, **46**(4), pp. 863–873.
- [5] Campobasso, M. S., Duta, M. C., and Giles, M. B., 2003, "Adjoint Calculation of Sensitivities of Turbomachinery Objective Functions," *J. Propul. Power.*, **19**(4), pp. 693–703.
- [6] Luo, J., Zhou, C., and Liu, F., 2014, "Multipoint Design Optimization of a Transonic Compressor Blade by Using An Adjoint Method," *ASME J. Turbomach.*, **136**(5), p. 051005.
- [7] Wang, D. X., and He, L., 2010, "Adjoint Aerodynamic Design Optimization for Blades in Multistage Turbomachines—Part I: Methodology and Verification," *ASME J. Turbomach.*, **132**(2), p. 021011.
- [8] Walther, B., and Nadarajah, S., 2015, "Adjoint-Based Constrained Aerodynamic Shape Optimization for Multistage Turbomachines," *J. Propul. Power.*, **31**(5), pp. 1298–1319.
- [9] Albring, T. A., Sagebaum, M., and Gauger, N. R., 2016, "Efficient Aerodynamic Design Using the Discrete Adjoint Method in Su2," 17th AIAA/ISSMO Multidisciplinary Analysis and Optimization Conference, Washington, DC, 13–17 June 2016.
- [10] Economou, D. T., Palacios, F., Copeland, S. R., Lukaczyk, T. W., and Alonso, J. J., 2015, "Su2: An Open-Source Suite for Multiphysics Simulation and Design," *AIAA J.*, **54**(3), pp. 828–846.
- [11] Sagebaum, M., Albring, T., and Gauger, N. R., 2017, Codipack – Code Differentiation Package | Scientific Computing.
- [12] Zhou, B. Y., Albring, T., Gauger, N. R., Ilario, T., Economou, D. T., and Alonso, J. J., 2017, "Reduction of Airframe Noise Components Using a Discrete Adjoint Approach," 18th AIAA/ISSMO Multidisciplinary Analysis and Optimization Conference, Denver, Colorado, June 5–9.
- [13] Sanchez, R., Palacios, R., Economou, D. T., Alonso, J. J., Albring, T., and Gauger, N. R., 2017, "Optimal Actuation of Dielectric Membrane Wings Using High-Fidelity Fluid-Structure Modelling," 58th AIAA/ASCE/AHS/ASC Structures, Structural Dynamics, and Materials Conference, Grapevine, TX, Jan. 9–13.
- [14] Vitale, S., Albring, T. A., Pini, M., Gauger, N. R., and Colonna, P., 2017, "Fully Turbulent Discrete Adjoint Solver for Non-Ideal Compressible Flow Applications," *J. Global Power Propulsion Soc.*, **1**(12), pp. 252–270.
- [15] Rubino, A., Pini, M., Colonna, P., Albring, T., Nimmagadda, S., Economou, D. T., and Alonso, J., 2018, "Adjoint-Based Fluid Dynamic Design Optimization in Quasi-Periodic Unsteady Flow Problems Using a Harmonic Balance Method," *J. Comput. Phys.*, **372**, 2018/06/26/09:26:31, pp. 220–235.
- [16] Young, J., 1984, "Semi-Analytical Techniques for Investigating Thermal Non-equilibrium Effects in Wet Steam Turbines," *Int. J. Heat Fluid Flow*, **5**(2), pp. 81–91.
- [17] Gyarmathy, G., 2005, "Nucleation of Steam in High-Pressure Nozzle Experiments," *Proc. Inst. Mech. Eng., Part A: J. Power Energy*, **219**(6), pp. 511–521.
- [18] Lettieri, C., Paxson, D., Spakovszky, Z., and Bryanston-Cross, P., 2017, "Characterization of Nonequilibrium Condensation of Supercritical Carbon Dioxide in a De Laval Nozzle," *ASME J. Eng. Gas. Turbines. Power.*, **140**(4), 11, p. 041701.
- [19] Starzmann, J., Casey, M. M., Mayer, J. F., and Sieverding, F., 2013, "Wetness Loss Prediction for a Low Pressure Steam Turbine Using Computational Fluid Dynamics," *Proc. Inst. Mech. Eng., Part A: J. Power Energy*, **228**(2), pp. 216–231.
- [20] Noori Rahim Abadi, S. M. A., Ahmadpour, A., Abadi, S. M. N. R., and Meyer, J. P., 2017, "Cfd-Based Shape Optimization of Steam Turbine Blade Cascade in Transonic Two Phase Flows," *Appl. Therm. Eng.*, **112**, pp. 1575–1589.
- [21] Jamali Keisari, S., and Shams, M., 2016, "Shape Optimization of Nucleating Wet-Steam Flow Nozzle," *Appl. Therm. Eng.*, **103**, pp. 812–820.
- [22] Hill, P., 1966, "Condensation of Water Vapour During Supersonic Expansion in Nozzles," *J. Fluid. Mech.*, **25**(3), pp. 593–620.
- [23] Economou, D. T., Palacios, F., Copeland, S. R., Lukaczyk, T. W., and Alonso, J. J., 2016, "SU2: An Open-Source Suite for Multiphysics Simulation and Design," *AIAA J.*, **54**(3), pp. 828–846.
- [24] Banach, S., 1922, "Sur Les Opérations Dans Les Ensembles Abstraits Et Leur Application Aux équations Intégrales," *Fundamenta Math.*, **3**, pp. 133–181.
- [25] Sagebaum, M., Albring, T., and Gauger, N. R., 2019, "High-Performance Derivative Computations using CoDiPack," *ACM Trans. Math. Softw.*, **45**(4), Article 38.
- [26] van der Stelt, T. P., Nannan, N. R., and Colonna, P., 2012, "The IPRSV Equation of State," *Fluid Phase Equilib.*, **330**, pp. 24–35.
- [27] Giordano, M., Hercus, S., and Cinnella, P., 2010, "Effects of Modelling Uncertainties in Condensing Wet-Steam Flows Through Supersonic Nozzles," V European Conference on Computational Fluid Dynamics ECCOMAS, Lisbon, Portugal, June 14–17.
- [28] Vargaftik, N. B., Volkov, B. N., and Voljak, L. D., 1983, "International Tables of the Surface Tension of Water," *J. Phys. Chem. Ref. Data.*, **12**(3), pp. 817–820.
- [29] Moore, M., and Sieverding, C., 1976, *Two-Phase Steam Flow in Turbines and Separators: Theory, Instrumentation, Engineering* (Series in Thermal and Fluids Engineering), Hemisphere Pub. Corp.
- [30] Starzmann, J., Casey, M. V., and Mayer, J. F., 2012, "Water Droplet Flow Paths and Droplet Deposition in Low Pressure Steam Turbines," High Performance Computing in Science and Engineering'12, Springer Berlin Heidelberg, Oct, pp. 351–365.
- [31] Kraft, D., 1998, A Software Package for Sequential Quadratic Programming. Technical Report, DLR German Aerospace Center — Institute for Flight Mechanics, Koln, Germany.
- [32] Dykas, S., Majkut, M., Strozik, M., and Smotka, K., 2015, "Experimental Study of Condensing Steam Flow in Nozzles and Linear Blade Cascade," *Int. J. Heat. Mass. Transfer.*, **80**, pp. 50–57.
- [33] White, A. J., Young, J. B., and Walters, P. T., 1996, "Experimental Validation of Condensing Flow Theory for a Stationary Cascade of Steam Turbine Blades," *Philos. Trans. R. Soc. A: Math., Phys. Eng. Sci.*, **354**(1704), pp. 59–88.
- [34] Gyarmathy, G., 1962, "Grundlagen Einer Theorie Der Naßdampfturbine," PhD thesis, Eidgenössischen technischen hochschule, Zurich.
- [35] Gerber, A., and Kermani, M., 2004, "A Pressure Based Eulerian–Eulerian Multi-Phase Model for Non-Equilibrium Condensation in Transonic Steam Flow," *Int. J. Heat. Mass. Transfer.*, **47**(10–11), pp. 2217–2231 Elsevier BV.